THE EFFECTS OF DOPING ON THE LITHIUM IONIC CONDUCTIVITY OF LLZO SOLID-STATE ELECTROLYTE

A Thesis
Submitted to the Graduate Faculty
of the
North Dakota State University
of Agriculture and Applied Science

By

Fadhilah Ahmed Altayaran

In Partial Fulfillment of the Requirements
for the Degree of
MASTER OF SCIENCE

Major Program:
Materials and Nanotechnology

November 2020

Fargo, North Dakota

North Dakota State University
Graduate School

Title

THE EFFECTS OF DOPING ON THE LITHIUM IONIC CONDUCTIVITY OF LLZO SOLID-STATE ELECTROLYTE

By

Fadhilah Ahmed Altayaran

The Supervisory Committee certifies that this ***disquisition*** complies with North Dakota State University's regulations and meets the accepted standards for the degree of

MASTER OF SCIENCE

SUPERVISORY COMMITTEE:

Dr. Qifeng Zhang
Chair

Dr. Erik Hobbie

Dr. Wenjie Xia

Dr. Danling Wang

Approved:

November 19, 2020 — Date

Dr. Erik Hobbie — Department Chair

ABSTRACT

Lithium-ion batteries (LIBs) employing solid-state electrolytes are considerably safer and might potentially generate a higher energy density compared. The goal of this thesis is to investigate the synthesis and stability of doped $Li_7La_3Zr_2O_{12}$ (LLZO). The reason of adopting LLZO is to presents a high conductivity, good electrochemical stability against metallic lithium. The investigation method involves preparing LLZO powder, pressing it to pellets, sintering the pellets at 1230 ºC and coating metal electrodes on them, followed by the measurement of the lithium ionic conductivity through Electrochemical Impedance Spectroscopy, Scanning Electron Microscopy, and X-ray diffraction. Doping has proven to be an effective way to improve the lithium ionic conductivity. In our research, multi-doped LLZO with Al and Ta and F presented the highest conductivity $\sigma = 1.67\times10^{-4}$ Scm^{-1} at room temperature. Our study suggests that the adoption may lead to a significant increase in the lithium ionic conductivity of LLZO solid-state electrolyte.

ACKNOWLEDGMENTS

I would first like to acknowledge the Ministry of Higher Education of Saudi Arabia and the Saudi Cultural Mission in the United States of America for giving me the opportunity of a full scholarship program at North Dakota State University and for all the support I was given to further my research, thank you.

I would like to acknowledge and express my extreme gratitude to my supervisor, Professor Qifeng Zhang, for inspiring my interest and advancing my knowledge in the development of innovative technologies. I want to thank you for your patience, insightful feedback, and efforts to bring my work to a higher standard future vision, thank you.

In addition, I am thankful to the Material and Nanotechnology Program at North Dakota State University led by Professor Erik Hobbie providing me with the opportunity to pursue a master degree. I am also grateful to my supervision committee members Professor Qifeng Zhang (Chair), Professor Erik Hobbie, Professor Wenjie Xia, and Professor Danling Wang for all help and support, thank you.

I would like to thank my research partner, Dr. Pingchun Guo, who was instrumental in defining the path of my research with a high level of knowledge. For that, I am very grateful, thank you.

I would like to thank my colleagues, Michael Johnson, Sudipto Saha, Obinna Ama, Md Razuan Hossain, Youli Wang, and Md Mozammal Raju, for their guidance through each stage of the research process, thank you.

A very warm thanks and gratitude go to my father, Professor Ahmed Altayaran, my mother Mrs. Fatimah Alrifai, and my husband, Mr. Md Alnami for their wise advice and warm care at all times, thank you.

DEDICATION

This dissertation is dedicated to my wonderful parents, husband, and my sweet boys.

TABLE OF CONTENTS

LIST OF TABLES

LIST OF FIGURES

LIST OF APPENDIX FIGURES

CHAPTER 1. INTRODUCTION TO SOLID STATE ELECTROLYTE

1.1. A Brief Classification of Energy

All around the world, energy is considered one of the most important matters in the lives of humans. The market demand for power sources persists and inflates as long as the ambition to obtain a high-quality standard of living exists, which raises with an increasing population [1]. The high human demand use energy from the natural sources makes researchers focus more on finding clear, clean, and more efficient energy sources to keep their lives convenient [1]. The general sources that human have used over the years are fossil fuels, such as natural gas, coal, nuclear energy, and petroleum, which have the worst environmental conditions or increasing carbon dioxide (CO_2), and surely that effects climatic consequences, [1] which generate global warming. The difficulty of finding available natural resources and the condition of CO_2 emissions makes the global market demand increase clean electrical energy storage sources, which would reduce or eliminate these emissions [1].

In the future of the renewable energy industry, energy storage will become one of the critical components of electronic equipment [2]. Without this energy storage revolution, the time and the industry of all kinds of electronic devices will not proceed [2] [3]. It is very important to have an energy source of constant frequency like lithium-ion (Li^+) batteries [2]. Because of the continuity of short power interruption, $80 billion have been wasted via the U.S. industry each year, as KH LaCommare et al. reported [2] [4]. In the meantime, most renewable energy sources are associated with energy storage equipment to make the device gain smooth output as required; if not it cannot be a provider of energy even when plugged into a network, like wind power at a West Virginia wind farm which has around 20-MW battery storage equipment [2] [5]. The

energy storage technology with metal-air batteries is the best idea for storing energy, and it has a promising future storage system based in electrochemistry [2] [6] [7].

There are two types of electrochemical energy considered to be the most dominant in energy storage; batteries and capacitors [2] [8] [9]. The energy stored in batteries and capacitors differs in how the electric charge is stored. In batteries, the electrical energy is stored as chemical energy, and in capacitors it is stored as the surface charges [2] [9]. Because of this, the features of these materials are different inside of chemical reactions [2] [9]. These reactions happen all over the volume of a solid, which requires a specific material design to allow the reacting species to enter all over the material and eliminate it later [2]. On the other hand, for the capacitor, the electric charge requires a large surface and the storage capacity is related to the surface area [2]. A hybrid between the two creates supercapacitors, which involve both surface charge and chemical reactions in the volume of the material [2] [10] [11].

Batteries are the most electrical energy storage, which is considered a type of electrochemical storage technology [1]. A synthetic battery made up of single electrochemical cells or more performs a current (I) at a voltage (V) for a time (Δt) [12]. The consumption quantity of current and/or time at the stored power in the battery can be raised by increasing the zone of connecting cells in parallel or increasing the electrodes; likewise, connecting cells in a series gives increasing voltage and the desirable power (P) as the formula $P = IV$ gives [12]. Li-ion battery is considered as an effective power storage device due to the advantages of a high gravimetric energy density of about 150 Wh kg^{-1} [1] [13] [14] and the wide voltage window from 2.5 V to 4.2 V based on the electrode materials [1]. Also, the high energy density will contribute to the design of batteries, making them lightweight, dischargeable and own an extended battery cycle life [1] [13].

Solid-state electrolytes have been developed over the past 30 years and give many applications to enhance our lives [15] [16]. They have high chemical stability and high ionic conductivity at room temperature [15] [16]. To find and give the resources for the development of solid state batteries (SSBs) technology, the estimated suggestions of SSEs have to be confirmed by suitable data in the next decade [17]. The competencies for holding and developing this ceramic technology or battery technology from the companies include helping to find resources for processing the battery, engaging the broad level, and examining failures to achieve a well-positioned technology [17]. The characterization and categorization of this type of battery is described in many books and hundreds of paper publications [18] [19]-[22]. In addition, during the improvement of this type of battery, scientists came to recognize the solid state battery as the better benefit batteries [23] [24]. In fact, the development of a high energy density Li^+ battery system relies on the development of the high-performance electrodes in the solid electrolytes and the chemistry of electrodes [17]. Various perspectives have been tackled with several views in the solid-state battery technology field [17] [25]-[34]. In one of these study "Recent advances in all-solid-state rechargeable lithium batteries", Sun et al. provided an overview of the improvement of solid-state batteries [17] [25]. Manthiram et al. summarized lithium battery technologies and the advantages of solid state electrolytes in their paper titled "Lithium battery chemistries enabled by solid-state electrolytes" [17] [26]. Professor John B. Goodenough proposed the ideas of rechargeable Li^+ batteries as positive electrodes [1] [35].

1.2. Lithium Ion Conductor of Garnet-Type $Li_7La_3Zr_2O_{12}$

Garnet expression originally corresponds to natural silicates [36]. The general and classical formula of their compound is $A_3B_2C_3O_{12}$ with the components of A, B, and C, respectively and it refers to 8-coordinate units including octahedral and tetrahedral cation crystal

structure sites [36]. This material is recognized to show various advantageous properties in some study areas such as material science or magnetic materials [17] [36]. The structural flexibility of a garnet substance lets different chemical exchanges increase to a large number of phases [36]. Especially, this material exhibits a high Li conductivity [3] [37] [38] making it a great candidate of the electrolyte for lithium batteries [36].

Significantly, the enormous advantages of efficiency performance materials based on size scaling are rising dramatically, wherefore, a wide range of applications and interdisciplinary materials are now prepared very widely into the nanoscale level based on these advantages [39]. Practically, solid-state Li^+ batteries can be fabricated by typical solid-state reactions, in which the internal resistance of the solid oxide electrolyte is not only from the bulk resistance but is also from the grain boundary resistance in view of the polycrystalline structure of the electrolyte [39]. Based on that, garnet-type Li^+ containing metal oxides have been discovered as a novel type of fast lithium-ion conductors [25] [40] [41]. These complex compounds reveal high Li^+ conductivity above ~10^{-6} Scm^{-1} at room temperature [40]-[44]. The SSBs, which use solid electrolytes, have received great attention because of the improvement in the safety, volumetric power, density, and flexibility creation [45]. Among the garnet-type LLZO solid electrolytes, the one with the formula $Li_7La_3Zr_2O_{12}$ (LLZO) has presented a promising generation, efficiency and much quality in the battery field and applications consequent to the effect of the high ionic conductivity of lithium [45]. In past decades, many types of solid-state electrolytes (SSEs) have been developed; for example, garnets, LiPON, perovskites, and sulfides, etc. [46] [47] LLZO is the only unique battery material that scientific researchers compete for, and presents an unrivalled combination of stability and high ionic conductivity against Li metal [48] [49]. The

materials of LLZO have been examined and studied on both theoretical and experimental sides [40] [50] [51].

In recent years, scientists made great efforts to improve the lithium-ion conductivity and the sinterability of garnet-type oxide [52]. They reported the investigation of the phase structure evolution during the sintering process and the high density of garnet-type electrolytes by situ neutron powder diffraction (NPD) analysis, which enables to reveal the synthesis sintering processes and accordingly obtain garnet-type electrolytes with a high dense [52] [53].

A sturdy understanding of SSE product establishment viewpoint is required to develop the cell's lifetime, the volumetrics and gravimetrics of cell power intensity on the basis, the product capacity of temperature condition tolerance, safety, and the material price [46] [54] [55]. Moreover, the significant prospective feature of SSEs is the ability to operate in both higher and lower temperatures [55]. In addition, using SSEs require knowledge of the availability of Li metal anodes and controlling the morphology of Li metal coating [55]. Specifically, the SSEs system decreased flammability, and subsequently increased the safety side, which gives another advantage to this system, though it requires more and continuous study [32] [55]. Unlike the fluid electrolyte systems which are currently used [16] [55], the voltage stability, the material component costs or the manufacturability of SSEs have not been well identified or clarified, and thus in evaluation of features might need to be considered as well as additional cost [55]. The handling and enhancing the operating lifetime of SSEs are also challenging [16] [55] [56].

1.3. The Mechanisms and Properties of A Solid-State Electrolyte

The electrical conductivity is a concept to indicate how good a given material is at conducting electricity [57]. Current is produced when electrical charges flow as various reactions in the electrical potential [57]. Determining the conductivity from this current, as calculated the

ratio of the density to the strength of the electric field is done, by measuring the resistance, area, and length of the sample [57]. Conductance is the reverse of resistance, and it measures the current generated via an element circuit for the applied amount of voltage [58] [59]. The conductance is measured in Siemens (S) and uses a sigma (σ) as the symbol [58] [59]. The conductance of a material depends on several factors, such as the shape, dimensions, and the conductivity or the property of the materials[58] [59]. For a pellet sample with the cross-sectional area A, the thickness d, and the resistance R, the conductivity (σ) is calculated as [58]

$$\sigma = \frac{d}{A.R} \qquad \text{(Eq. 1)}$$

The mechanisms of ion conduction solid-state conductors are remarkably different from liquid electrolytes [60]-[76]. Li^+ transfer in classic liquid electrolytes by moving solvated Li^+ in the solvent medium [60] [61]. Li^+ conductivity can be increased by increasing ion dissociation in solvents with considerable dielectric constants, and further promoting the Li+ mobility by lowering the viscosity by the Stokes-Einstein equation [60] [61]. In stoichiometric ion conductors, the ionic conductivity of crystalline solids is controlled by the number of interstitials, occupancy on lattice sites, and vacancies, which is specified by defect formation energy or the ionic energy gap, known as the intrinsic regime [60]. In addition, vacancies and interstitials can be formed by the extrinsic regime, which is substitution of aliovalent cations whose evolution energetics is controlled by the trapping energy (E_t) [60] [62]. In both regimes, the activation energy (E_a) of ion conductivity includes both contributions, which is migration energy (E_m) and defect formation energy (E_f) or (E_t) [60]. Although it is possible to increase the Li^+ conductivity with more concentrations of mobile Li^+ via aliovalent substitution to produce vacancies or interstitial atoms [60] [63]. The ions often move through the maximum point and start to reduction as much mobile types are added inside the lattice, where Li^+ ions are clearly interacting

and the mobility is no longer available independently [60] [63]. On the other hand, with the structural deformation produced by extrinsic defects or passing the typical concentration of mobile ions or by the substitution, result to decrease of the ionic conductivity past the typical aliovalent substitution and increases in the migration energy associated [60]. Over a critical concentration of substitution, the deformation of the crystalline lattice is highly solid and strong, which is perform from the increase of migration energy or decrease the extrinsic defects [60].

1.4. Crystal Structures of Garnet-Type Lithium-Ion Conductor

Due to high electrochemical stability and low electronic conductivity, lithium crystals of a garnet-type structure are consider perfect candidates for battery electrolyte materials [64]-[66]. Therefore, scientists have made lots of efforts on electrolyte materials to improve the power density of advanced lithium batteries [23] [64] [67]. Scientists have investigated a huge number of inorganic oxides and non-oxides, which display the amorphous and crystalline structures of this garnet type [23] [24].

Several mathematical and mechanism studies of Li^+ cells have been published [68]-[71]. The mathematical design of solid-state batteries has become a valuable instrument to clearly examine many phenomena that move during charge and discharge and find new or alternative materials with low activation energy, and low diffusion barriers of the position of positive ions, for instance, Li^+, Na^+ , Be^{2+}, Mg^{2+} ions [64]. Typically, to clarify the ions mobility of solid-state ions conductors, it is made up of mobile ions with metal and non-metal ions from many plane faces or (polyhedra) with molecule coordinate bonding (ligands) which generate the crystal structure [60]. Long ago, more than 50% of the components in the periodic table were exploited theoretically and experimentally in solid-state conductors [60]. Figure 1 shows a number of elements shaded with green, orange, and blue: cations and anions are shaded with green, and

ligands are in orange, and they have been applied to give the crystal structures, and the element supporting the ionic conduction in blue. Ligands, cations and anions such as H^+, Li^+, Na+, K^+, Mg^{2+}, Cu^{2+}, Ag^+, O^{2-}, F^- and Cl^- have been described to be mobile in solids [60]. In general, the ideal high ionic conductor was silver iodide (AgI), and this was the first element with high ionic conductivity solid-state ion conductors [60] [72], and sodium-ion-conducting (β-alumina) which came after [60] [73], and sodium (Na) or NASICON, and then a number of fast lithium-ion conductors [74] [75].

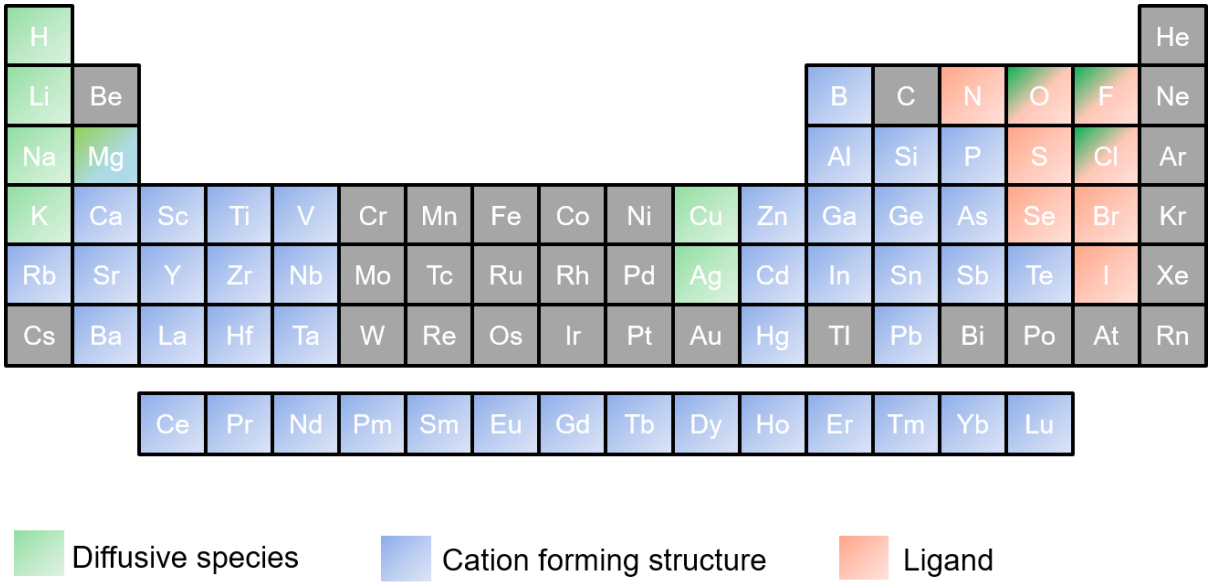

Figure 1. The periodic element table of cations and anions shaded in green and ligands in orange, and they have been applied to give the crystal structures and support ionic conduction in blue. [60]

1.4.1. Crystal Structures of Pure LLZO

The solid-state conductors vary from liquid electrolytes in the area of ion-conduction mechanisms [60]. The procedures of moving lithium ions in a liquid solvent are related to Li^+ transport [60] [61]. In past scientific studies, the cubic phase LLZO stabilization from the inclusion of doping elements was proven [21] [32] [77]-[80]. The structure of garnet-type Li^+ crystals is a good candidate in the battery electrolyte materials because it has comparatively low

electronic conductivity and high electrochemical stability [64] [66]. Until now, the Li garnet-type LLZO has been widely studied, finding various advantages [79]. In 2007, Murugan gave the first report of solid-state electrolyte LLZO [50] [81]. Numerous studies at the recent period indicate that LLZO has two diverse structures, which are cubic structure and tetragonal structure, respectively [50] [65] [81]-[83]. Since the extensive beginning study of the Li garnet-type LLZO [50] [79], it has been demonstrated that LLZO shows high Li ionic conductivity and low grain boundary resistance; moreover, LLZO is relatively stable in the ambient air and has superior chemical stability to Li metal [21] [32] [50] [78] [79] [82] [84]. The cubic and the tetragonal phase are the two structure phase forms of LLZO and the conductivity of the cubic phase, as many reported, showed about ~10^{-4} Scm^{-1} at room temperature, which is about two orders of magnitude higher than that of the tetragonal phase; the latter is about ~10^{-6} Scm^{-1} at room temperature [21] [32] [50] [78] [79] [82] [85]. Typically, to gain or achieve the cubic structure, all that is needed is several complex calcination steps, a long sintering time above 24 h or so, and a temperature range between 1000 ˚C to 1200 ˚C [21] [50] [78] [79] [82] [84]. The high-temperature thermal process causes a notable Li^+ loss to unavoidably occur, which breaks down the structure of LLZO for the formation of $La_2Zr_2O_7$ or other second phases [50] [78] [79] [82] [86]. In that way, the decrease of ionic conductivity accrues [50] [78] [79] [82] [86]. It is difficult to synthesize the pure cubic structure of LLZO without getting secondary phases of $La_2Zr_2O_7$ at room temperature because the cubic LLZO is not stable as many reported [87] [88]. The cubic structure of pure LLZO considered unstable and tends to alter into the tetragonal phase structure at room temperature [81]. The observed amount of Li^+ tetragonal structural conductivity is comparable with several big groups of complex structural compounds [25] [32] [50] [89]-[93].

Figure 2 shows the crystal structures of the solid-state Li^+ electrolyte material LLZO [64]. The crystal structure of LLZO is a tetragonal structure and the unit cell of the tetragonal modification 1.31 nm for (a) and (b), and 1.27 nm for (c) showing the space group number 142 with symmetry of I41/acd [29]. $Li_7La_3Zr_2O_{12}$ has 8 formula units and 56 lithium atoms within three various crystallographic sites [29]. Figure 2a shows position 1 of Li and it has 8 atoms at the tetrahedral (4 nearest-neighbours oxygen atoms = 1.89 Å for each), Figure 2b shows position 2, Li has 16 atoms at the octahedral (6 nearest-neighbours oxygen atoms = 4 nearest neighbours atoms = 1.93 Å, 1.93 Å, 2.34 Å, 2.34 Å, 2.44 Å, and 2.44 Å), lastly, Figure 2c shows position 3, Li has 32 atoms at the minus symmetrical tetrahedral (4 nearest-neighbors oxygen atoms = 1.85 Å, 2.02 Å, 2.04 Å, and 2.17 Å) [64] [77]. The influence of these three various kinds of Li-atoms on the diffusion properties (the coefficients and activation energies) was investigated theoretically as a temperature function and total lithium concentration from using the ab initio density functional theory [64] [94]-[96].

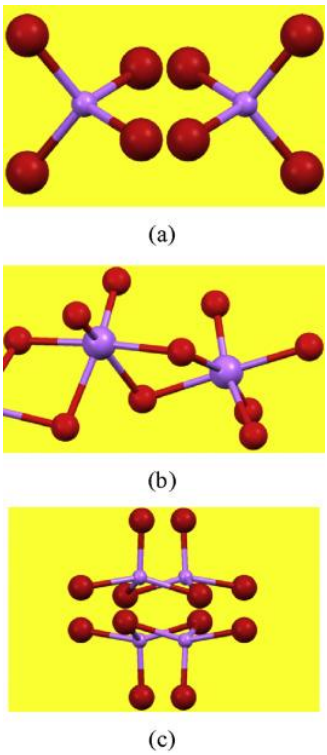

Figure 2. The crystal structures of tetragonal LLZO, lithium Li^+ (purple), and the nearest-neighbour is oxygen particles (red) of lithium at (a) position 1, (b) position 2, and (c) position 3. [64]

In more detail, various structural forms for LLZO have been reported: first, cubic phase Ia-3d or I-43d space group at a high temperature [50] [97] [98] with tetragonal structure I41/acd space group at a high temperature [97] [99], and second, tetragonal structure I41/acd space group at a low temperature [97] [100] [101]. The ionic conductivity depends on multiple parameters, especially lithium concentration which is related to the structure of lithium site occupancy ratios among tetragonal and octahedral phases and the doping level [98] [102]. There is no Li vacancy in the tetragonal phase structure of pure-LLZO at low temperatures, and this causes a low Li ionic conductivity [103]. There are three various sites of Li^+ occupation regarding the tetragonal phase; the first Li^+ is tetrahedral-8a, the second Li^+ is octahedral-16f, and the third Li^+ is 32 g, respectively [99] [103]. On the other hand, tetragonal LLZO converts into the cubic phase when the temperature is increased more than 650 °C as some reported [103] [104]. There are two

disordered Li vacancies that form in the cubic phase, which are tetrahedral-24d as the first Li^+ site, and octahedral-96h as the second Li^+ site [99] [103]. From that, cubic phase characteristics can open the pathway of Li diffusion and clearly improve Li-ionic conductivity around ~10^{-3} and 10^{-4} Scm^{-1} [103] [105] [106].

Moreover, at room temperature, changing the lithium and zirconium sites provides a promising strategy to stabilize the high conductive cubic structure phase and increase the conductivity of an Li^+ garnet [98] [107] [108]. Using the approximate temperature from 700 ºC to 900 ºC, can obtain a tetragonal structure easily by solid-state reaction synthesis without doping and give a lower ionic conductivity by twice the magnitude as compared to the high-temperature cubic phase [97]. In addition, the lower sintering temperatures e.g., ~ 800 ºC, typically result in a low Li^+ conductivity [97]. At the higher sintering temperatures, between 1100 ºC to 1300 ºC, the lithium ionic conductivity of cubic garnet LLZO is approximately ~10^{-4} Scm^{-1} and the material presents a stable cubic structure [97]. The hard stabilization of the cubic phase is without any doping, the elements doping such as Al, Ta [32] [97], Nb, [21] [97] and Ga. [97]. Chen et al. found that Al-doped specifically can assist and facilitate getting densification during the sintering process [97] [109].

1.4.2. Crystal Structures of Al-Doped LLZO

In solid-state electrolytes, the ionic transport properties are closely related to the microstructures and chemical compositions [43] [110]. An example of this is, in Al substituted LLZO, both lithium and aluminum contents are sensitive to the treatment temperatures and the heating time of the sintering process [110] [111]. The scientists' effort for modifying the microstructure is to change the synthetic routes or processing conditions that cause variations in the material composition of the densified ceramic [110]. This regards the spacious distribution of

chemical compositions and microstructures for LLZO samples which is reported in the literature papers [110] [112] [113]. There are limitations in the knowledge of the relationships between the crystal microstructure, interfacial resistance, and cycling life production, despite the efforts in the microstructure engineering of solid-state electrolytes [110]. The understanding of the electrochemical conduct of solid electrolytes of LLZO is a massive challenge in the case of interfaces, bulk, and microstructure effects of chemical composition [110].

The stabilization of the cubic structure LLZO at room temperature is achieved by using the dope methods of elements such as aluminum (Al), which may else enhance the ionic-conductivity [65] [81] [83] [114] [115]. Application of different dopants, such as Al, Ta, Ga, Mo, and Nb was introduced at the lattice of LLZO with the Li^+ pathway; dramatically, Li^+ conductivity was increased due to the dopant effect from 10^{-7} to 10^{-4} Scm^{-1} [21] [50] [52] [107] [116] [117]. Nevertheless, the garnet type electrolyte LLZO still owns conduction poorer than that of commercial liquid electrolytes, resulting in a worse performance in the side of electrochemical performance, particularly, at an elevated charge or discharge of current density and at ambient temperature [52]. Figure 3 indicates that at the time an un-doped cubic phase keeps the conduction paths of Li-ions in both Figure 3a and Figure 3b then the occupancy of Al in the Li sites indicatively blocks the connecting paths [118]. In more detail, the conduction of Li-ions is blocked by Al in the 24d at intersection sites Figure 3c for the incoming Li ions from four different directions, while only the one-way pathway of Li-ions is blocked by the Al in the 96 h sites Figure 3d [118]. This refers to the Li that conductivity would be more susceptive of Al in the 24 d sites than that in the 96 h sites, even for the same quantity of Al dopants [118]. During the thermal reaction, the Al gets contamination from the alumina crucible, and that plays an important role in stabilizing the cubic LLZO, as Geiger et al. mentioned [118] [119]. In

addition, adding the Al element has succeeded in accelerating the formation of cubic LLZO structure [32] [85] [118] [120]. Additionally, this reaction can also increase the relative density [97]. Chen et al. found that Al-doped specifically could assist and facilitate getting densification during the sintering process [97] [109].

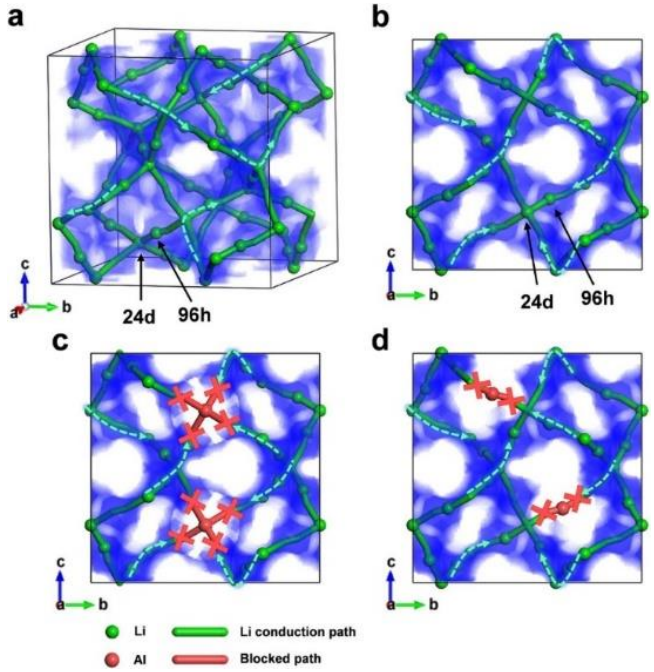

Figure 3. 3D sketch representation of pure LLZO and Al at the blocking effect in a cubic LLZO structure (a) un-doped cubic LLZO (b) the [100] direction of un-doped cubic LLZO, (c) Al-doped LLZO in 24 d site, and (d) Al-doped LLZO in 96 h site. Remarkable is the red sign "X" in both (c) and (d) for the blocked paths by Al, and green arrows indicate the diffusive motion of Li. [118]

1.4.3. Crystal Structures of F-Doped LLZO

In order to gain high conductivity from doping with different elements, the solid electrolytes should have high density, which generally means high ionic conductivity [81]. The element fluorine, which might form a lithium fluoride compound, can enhance the performance of the crystal structure and can be a sintering aid in the formation of the cubic garnet phase [121]. The unique microstructure of garnet-type lithium is exhibited when it is doped with fluorine [121]. Applying 40% of fluorine can form a net structure of closed pores in the sintered

lithium garnet [121]. The closed porosity plays an important role to get higher ionic conductivity and a lot of solid microstructure surface [121]. However, it has been also pointed out that applying more than 40% fluorine may result in an undesired phase or a second formation phase of $LaZr_2O_7$ [121].

To enhance the poor conduction of tetragonal $Li_7La_3Zr_2O_{12}$ by converting it to cubic phase to thus gain high conduction at lower temperatures, doping is an ideal method to tailor the Li content, which affects Li vacancies and disrupts the range of the Li order [122]. This can be performed through doping [32] [122] [123] on the Li site or on the Zr site [32] [122] [124]. In fact, at high temperatures, the reaction between the garnet powders and alumina crucible can dope Al unintentionally [118] [122] [124] [125]. Recently, scientists investigated the effects of doping materials such as fluorine in lithium electrolyte materials [45] [122] [126]. Including fluorine ions with LLZO in the synthesis process will contribute and enhance the stabilization of the cubic phase to exhibit a total conductivity of $\sim 5\times10^{-4}$ Scm^{-1} [45] [122]. Using fluorine as an incorporation within the garnet structure is truly a new approach to improve ionic conductivity, and thus this novel approach reveals the pathways and diffusion techniques taking place [122]. LLZO doped with fluorine is an analogy to pure cubic LLZO, which has been beneficial for stabilizing the cubic phase structure [45]. Li^+ conductivity and fraction numbers of Li vacancies might be affected by lowering dopant levels [45]. At the same time, it helped to release lithium sites of the octahedral, which likely results in the stability of the cubic garnet phase at room temperature [45].

For further understanding, R. Yeandel et al. presented the comparison between the lattice parameters of the pure LLZO system and the F-doped LLZO system [122] The pure LLZO system is tetragonal between 26 ºC and 430 ºC, suggesting the structure is either fast

interconverting to orthorhombic forms or the Li-site has dual potential and is determined to a single minimum [122]. At 430 ºC, the pure LLZO structure has become cubic, and to a limited extent the pure structure tetragonal LLZO has no humidity and it undergoes a reversible phase transference to the cubic phase at nearly 630 ºC [122] [127] [128]. The variation of phase transference is referred to the complexity and difficulty of obtaining accurate phase transference temperatures [122]. On the other hand, the F-doped LLZO system is largely cubic with inconsequential deviations across the full area of temperatures [122]. The minor deviations from the cubic structure are completely constant at all temperatures; therefore, they attributed to the randomness of the distribution of the fluorine defects [122]. Consequently, the work of Cai et al. suggests that the LLZO cubic phase is stabilized at low temperatures because of the combination of fluorine induced defects [45] [122]. The investigation of the ionic conductivity Li-battery applications leads to preference of the cubic phase to get high ionic conductivity, resulting in F-doping LLZO [122]. Moreover, the lithium density of both systems, the pure LLZO and F-doped LLZO system displayed in Figure 4. Figure 4a shows the pure-LLZO system as an isolated sketch of lithium density at 230 ºC, specifying to a rare hopping of lithium from one site to the other [122]. Figure 4b shows the F-dope LLZO ions. The isolated sketch is much connected, which makes the movement of lithium from site to another much easy [122]. Figure 4c shows the pure LLZO system transference into the cubic structure at 730 ºC, and the pathways of lithium density were completely connected together, which specifies free lithium ion movement between all sites [122]. Furthermore, Figure 4d shows at 730 ºC, the F-doped system also contributes to an increase in pathway connectivity but refers to a lower connective rung in the pure system [122]. At both situations, Li transition is completed through a vacancy hopping mechanism [122]. Also, due to the stabilization of the cubic phase, the study suggests the incorporation of

fluorine defects to recover lithium vacancies, which leads to increased lithium diffusion at lower temperatures; however, reduced lithium diffusion at higher temperatures is due to the movement of lithium vacancies by fluorine defects [122]. Note that the experimental investigation of F-doped LLZO has not been reported yet, and in our work we explored and achieved better results experimentally and compare with the simulation part.

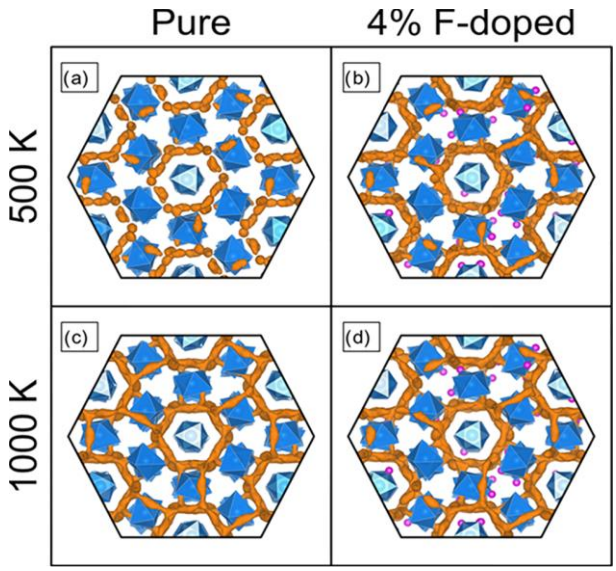

Figure 4. Schematic pathways of lithium-diffusion LLZO (a) and (b) display the pathways of pure LLZO and F-doped LLZO systems at ~230 ºC (500 K), respectively; (c) and (d) display the pathways of pure LLZO and F-doped LLZO systems at ~730 ºC (1000 K), respectively. Lithium-diffusion pathways colored (brown), (blue) for zirconium octahedral, and (pink) for fluorine ions. [122]

1.4.4. Multiple Doping of LLZO and Al and F Co-Doped LLZO

Decreasing the interface resistance and increasing the bulk ionic conductivity are useful strategies to improve the overall lithium ionic conductivity of solid electrolytes [129]. Studies showed that to increase the bulk ionic conductivity of LLZO, the lattice of garnet-type should be replaced with individual elemental substitution to introduce Li^+ vacancies [21] [121] [130] [131]. Furthermore, other studies found that lithium ionic conductivity was also increased by the binary substitution, which led the substitution move into the La site and increased the occupation of the Li site of garnet-type LLZO [39] [129] [132] [133]. Since the stabilization of the cubic structure

of garnet type is critical importance to enhance the densification of the solid electrolyte, an efficient way to stabilize the structure of garnet type LLZO in the cubic phase is to apply partial substitution by various cations, such as Al and Ge, [129] [134] [135] or Al and F.

Improving the properties of practical materials may come from applying the combined doping of the garnet type LLZO [129]. This way is a useful strategy that inserts a synergistic influence that is barely achieved by single or individual doping [129]. In addition, combined doping can be achieved on the same or different cation site, which could significantly enhance the activity and stability for the oxygen reduction reaction at certain temperatures [129] [136] [137]. Using the combined substitute dope element has been demonstrated to be a perfect candidate as an anode for solid-state Li^+ batteries [52]. Compared with fluorine anions and oxygen ions, fluorine anions have a high electronegativity [52]. There are no publication papers that have mentioned the combination dope LLZO with Al and F^-, except an example by Yao Lu. et al. with Gallium (Ga) and fluorine (F), which revealed that the appropriate Li^+ diffusion pathway could be composed in garnet-type $Li_{6.25}Ga_{0.25}$ $La_3Zr_2O_{12}$ (LGLZO) through the partial substitution of oxygen via fluorine, resulting in $Li_{6.25}Ga_{0.25}La_3Zr_2O_{12}F$ [52]. It was explained that the doping of the crystal lattice by fluorine indicates lowers the displacements of atoms, and thus makes the paths of Li^+ faster and the microstructure of the pellets much dense' and smoother [52]. As a result, a high ionic conductivity was obtained as 1.28×10^{-3} Scm^{-1} at room temperature which comes from less resistance and the observation of stability, and it was noticed that the samples were much more stable than if a single element dopant had been applied [52].

Currently, the experimental part of doping Al and F into the garnet-type LLZO has not been reported yet. In addition, we investigated the phase structure of Al and F-doped LLZO, the

densification, conductivity, and the performance of the electrolyte for solid-state Li^+ batteries experimentally.

1.5. The Stability of LLZO in H_2O, CO_2 and/or Ethanol Exposure

The crucial understanding point of garnet-type LLZO is the stabilization of the correct phase [98]. While the pellet samples may have the required chemistry and phase transition, the structure can affect lithium loss during the annealing process, resulting in the destabilization of the phase [98]. Presently, all lithium-type garnets are considered chemically stable while being exposed to moisture and air [36] [138] [139]. And as some reported literature papers claimed that the garnet type of LLZO is chemically stable against moisture [130] [140] [141], other reports showed Li^+ conducting oxides [130] [142] [143]. More research studies have concluded that the garnet type of LLZO is chemically unstable against moisture through a replacement process of lithium-ions by protons under the condition of the ambient air humidity [130] [143] [144], or immersion of the materials in a solvent of water [123] [130] [143] [145]. Actually, the replacement reaction has a beneficial impact on the conductivity of un-doped LLZO [130]. In the tetragonal phase of LLZO, the high lithium concentration and the closeness of available sites impose the organization into this phase, which causes the replacement of lithium ions in the LLZO lattice by protons, which destabilizes the Li organization with a Li-ion filled garnet structure and raises the structure of cubic LLZO [130] [145]. For instance, Nyman et al. emphasized the instability of garnet associated electrolytes in relation with moisture for the first time by confirming the exchange between H^+ and Li^+ in $Li_5La_3Ta_2O_{12}$ and $Li_5La_3Nb_2O_{12}$ that immersed in the solvent (water), which ends with $Li_{5x}H_xLa_3Ta_2O_{12}$ and $Li_{5x}H_xLa_3Nb_2O_{12}$ forming the partially protonated analogy [145] [146]. This, along with Truong et al. proved that the Li stuffed garnets on the Ta-analogue demonstrate higher chemical stability in the solvent

(water) due to solid Ta and O bonds [147] [148]. Moreover, the reaction between water and grant LLZO will cause an ion-exchange issue of Li^+ and H^+ that delivers LiOH [7] [144] [149] [150]. Water pH amount can be raised from 7 to 11 or above right away after the reaction with a small amount of Li garnet powder [7]. The description of this reaction such as between water and LLZO would be such as $Li_7La_3Zr_2O_{12} + {}_xH_2O \rightarrow Li_{7-x}H_xLa_3Zr_2O_{12} + {}_xLiOH$ [7]. Thus, the method of using water solvent can make the surface of the structure solid enough; however, since the chemical ion-exchange happened it caused a thermally unstable material, which decomposes during the annealing process [7].

Lithium compounds, such as lithium hydroxide (LiOH), can removed partially from the garnet component of pure lithium at room temperature when the chemical reaction happens from the air and ethanol solvent exposure [139] [151]. This reaction depends on the time and temperature that the samples are exposed to [151]. Tomohiro Furukawa et al. mentioned that the major impurity found during ethanol exposure was the carbon (C) component [139].] Figure 5 shows an image of the behaviour of a LiOH compound exposed to ethanol at 30 °C. As noticed in this figure, the original color on the surface of LiOH samples did not change from the white color upon exposure to ethanol at the same temperature 30 ºC for different times, and there was no surface exfoliation change [139]. The main finding is the weight loss with the density of the samples, thus the ethanol could play an observable role to change the content of Li component [139]. Unfortunately, there is no information published yet regarding temperature effect during the ethanol exposure [139].

Figure 5. The change of phases of a lithium hydroxide compound during exposure to ethanol at 30 °C. [151]

The standard procedure includes high-temperature annealing in the Al_2O_3 crucible in air [143]. Some reports mentioned that the unintentional introduction of Al_2O_3 crucible was responsible for the observed cubic phase [98] [143] [152] However, Al cubic LLZO has been reported as well [100] [105] [143]. It was found that tetragonal LLZO can be converted into a cubic phase after a period of time in the air [119] [143]. In addition, this is similar to tetragonal cubic phase transformation observed naturally through time (aging time) [143] [146]. Regarding this, it is critical to control both the alumina contamination and air exposure within the synthesis process in order to totally recognize the phase transitions of LLZO [143]. In general, the impacts of exposure to H_2O and CO_2 are unclear so far, in the way how the transport properties impact Li conducting garnets [143]. Finding and understanding this technological knowledge of garnet-type solid electrolytes in lithium batteries is highly important to create stability and contamination-free samples and understand the phase transition of LLZO [143]. The LLZO component elements known as lanthanum (La) and zirconium (Zr) have inefficient oxidation at a low capability against Li^+ [48]. The synthesis methods of this type of LLZO electrolytes are usually performed in the air by the sintering process [48]. From that, they are comparatively stable in ambient air [48]. This combination of stability that comes from the thermal, chemical and electrochemical of LLZO might highly simplify fabrication and greatly improve the safety [48] [91] [132] [153].

1.6. This Study

In our work, we investigated the effects of doping on the lithium ionic conductivity of $Li_7La_3Zr_2O_{12}$ (LLZO). The materials were synthesized through a solid-state reaction. They were made into pellets and sintered at 1230 ºC to achieve the compositions as follows:

$Li_7La_3Zr_2O_{12}$

$Li_7Al_{0.2}La_3Zr_2O_{12}$

$Li_7La_3Zr_2O_{12}F_2$

$Li_{6.4}La_3Zr_{1.4}Ta_{0.6}O_{12}$

$Li_{6.7}La_3Zr_{1.7}Ta_{0.3}O_{11.5}F_{0.5}$

$Li_{6.7}Al_{0.1}La_3Zr_2O_{11.5}F_1$

$Li_{6.4}Al_{0.1}La_3Zr_{1.7}Ta_{0.3}O_{12}$

$Li_{6.6}Al_{0.06}La_3Zr_{1.8}Ta_{0.2}O_{11.67}F_{0.67}$

With these samples, we achieved the highest lithium ionic conductivity $\sigma \approx 1.67\times10^{-4}$ Scm^{-1} with $Li_{6.6}Al_{0.06}La_3Zr_{1.8}Ta_{0.2}O_{11.67}F_{0.67}$.

CHAPTER 2. EXPERIMENTAL OPERATION

2.1. Materials Preparation and Methods

The methods of preparation of LLZO solid-state electrolytes are in two major procedures. The first is to prepare precursor powder also called the mother powder, and the second is to make pellets with the precursor powder. In a typical way, the preparation of the precursor powder was done with a solid-state reaction. The pellets were prepared using a press technique for consolidation before sintering. Permanently, the main categorization for the method of preparation of LLZO pellets is known as the press method, which is performed upon the LLZO pellets and gives them a higher density. However, many reports estimate the cold-pressing process even promoted the pressure to a high standard level such as 800 MPa; however, the density for tetragonal LLZO reported in this case was as lows level as 73% [77] [81] [154]. In short, the preparation of LLZO powder using the solid-state reaction with the exact procedure from the precursor materials ends up with making the pellets.

The stoichiometric ratio amount of the powder materials was weighed for LiOH 98% (from Bean Town Chemical BTC), La_2O_3 99.9% (from TCI America Co. LTD), ZrO_2 99% (from Spectrum Chemical MFG), Al_2O_3 99% (from Alfa Aesar), LiF 98.5% (from Alfa Aesar), and Ta 99% (from Bean Town Chemical BTC), The formulas used for pure-LLZO, Al-LLZO, F-LLZO, Ta-LLZO, Al and F co-doped -LLZO, Ta and F-LLZO, Al and Ta-LLZO, and Al and Ta and F-multi-doped LLZO, are $Li_7La_3Zr_2O_{12}$, $Li_7Al_{0.2}La_3Zr_2O_{12}$, $Li_7La_3Zr_2O_{12}F_2$, $Li_{6.4}La_3Zr_{1.4}Ta_{0.6}O_{12}$, $Li_{6.7}La_3Zr_{1.7}Ta_{0.3}O_{11.5}F_{0.5}$, $Li_{6.7}Al_{0.1}La_3Zr_2O_{11.5}F_1$, $Li_{6.4}Al_{0.1}La_3Zr_{1.7}Ta_{0.3}O_{12}$, and $Li_{6.6}Al_{0.06}La_3Zr_{1.8}Ta_{0.2}O_{11.67}F_{0.67}$, respectively. The molar ratio of these samples elements are (Li^+ : La^{3+} : Zr^{2+} is 7 : 3 : 2), (Li^+ : Al^{3+}: La^{3+} : Zr^{2+} is 7 : 0.2 : 3 : 2), (Li^+ : La^{3+} : Zr^{2+} : F is 7 : 3 : 2 : 2), (Li^+ : La^{3+} : Zr^{2+} : Ta is 6.4 : 3 : 1.4 : 0.6), (Li^+ : La^{3+} : Zr^{2+} : Ta : F is 6.7 : 3 : 1.7 : 0.3 : 0.5),

(Li^+ : Al^{3+} : La^{3+} : Zr^{2+} : F is 6.7 : 0.1 : 3 : 2 : 1), (Li^+ : Al^{3+} : La^{3+} : Zr^{2+} : Ta is 6.4 : 0.1 : 3 : 1.7 : 0.3), and (Li^+ : Al^{3+} : La^{3+} : Zr^{2+} : Ta : F is 6.6 : 0.06 : 3 : 1.8 : 0.2 : 0.67), respectively. The amount of the materials after calculated per 1 gram is shown in in Table 1. After the stoichiometric ratio was weighed, a corundum crucible Al_2O_3 was used and placed into the muffle furnace (VIV-MBF1700-V03) at 900 ºC for 8 h to decompose the Li metal and get the LLZO powder. Note that there was no addition of LiOH with the mixture at this point to avoid the Li loss during annealing. After the annealing step, the powder was mixed with LiOH powder and around 8-10 ml of isopropanol alcohol (C_3H_8O) was added as a solvent. The planetary zirconium Ball Mill (PBM-04) was used for 5 h at 400 rpm resolution per minute. The oven was used to dry and calcine the slurries overnight, or about 24 h at 65 ºC. The synthesized powder was grounded using a mortar and pestle, followed by the sieve (METRIC: 106 µm and INCH: 0.0041) to get a smooth powder. A hydraulic press was used at 9 US-Tons and a stainless steel tool (EQ Die 12D-B) was used to press the collected mixture powder into pellets. The thickness of the pellets is 1.0 mm for each 1 g of the amount of the resulting powder. The pellets were placed in an Al_2O_3 crucible and covered with the mother powder to reduce the evaporation or loss of Li during the anneal treatment. Finally, the pellets were sintered at 1230 ºC for 8 h to obtain a fully dense body and develop the grains of LLZO. After the sintering, the pellets were polished using sandpaper sheets to remove small pieces on the surface, and then compressed air was used to remove any extra composition particles. The coater (Torr international, INC.) was used to spatter both surface sides of all polished pellets with titanium (Ti) as Li^+ blocking electrodes, to coat the substance pellet surface and create the electrode. Figure 6 shows the sample preparation and measurement methods.

Table 1. A summary of the formulas of the tested samples and chemical recipes per gram.

Sample Formula / chemical compositions (1g)	LiOH	La_2O_3	Zr_3O_2	Al_2O_3	Ta	F
$Li_7La_3Zr_2O_{12}$	0.18569	0.54133	0.27296	-	-	-
$Li_7Al_{0.2}La_3Zr_2O_{12}$	0.17057	0.54384	0.01134	0.27423	-	-
$Li_7La_3Zr_2O_{12}F_2$	0.17560	0.51191	0.25813	-	-	0.05434
$Li_{6.4}La_3Zr_{1.4}Ta_{0.6}O_{12}$	0.16605	0.52944	0.18688	-	0.11761	-
$Li_{6.7}La_3Zr_{1.7}Ta_{0.3}O_{11.5}F_{0.5}$	0.17108	0.52107	0.22333	-	0.07067	0.01382
$Li_{6.7}Al_{0.1}La_3Zr_2O_{11.5}F_1$	0.17316	0.52739	0.26594	0.00550	-	0.02799
$Li_{6.4}Al_{0.1}La_3Zr_{1.7}Ta_{0.3}O_{12}$	0.16609	0.52957	0.22698	0.00552	0.07182	-
$Li_{6.6}Al_{0.06}La_3Zr_{1.8}Ta_{0.2}O_{11.67}F_{0.67}$	0.16931	0.52349	0.23757	0.00365	0.04733	0.01861

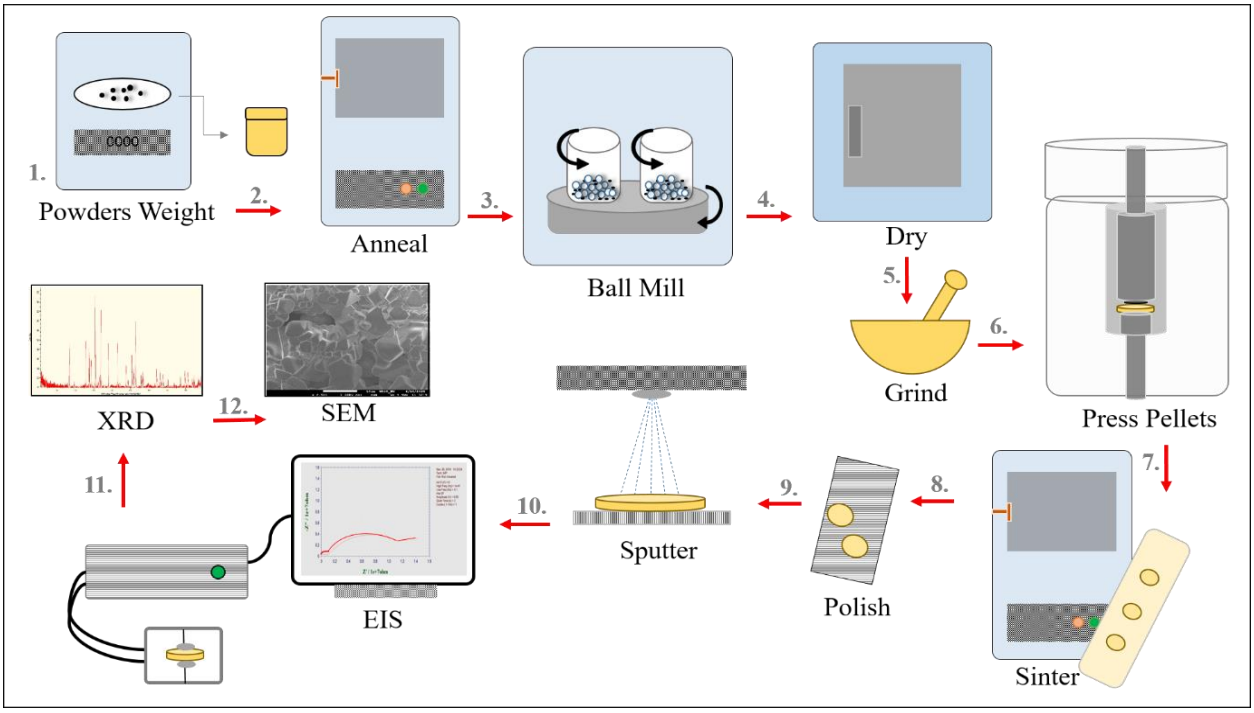

Figure 6. Schematic drawing showing the preparation and measurement methods used in our study.

2.2. Material Characterizations

Solid materials can be characterized in different ways, such as elemental analysis, spectroscopic, SEM/TEM microscopic, X-ray diffraction, and electrochemical techniques [155]. The electrochemical technique has been significant for the research/study of insertion processes in battery materials [155]. Electrochemical characteristics and electrochemistry can provide and

supplement analytical information, which has allowed the identification of structural phases, discovery of various solid species, and the homogeneity of the sample [155]. There are important points of electrochemical characteristics that have not been completely explored or understood, such as the formal potentials for redox pairs of solid-state materials as an indication of the solution environment and the capability of the solids to go through reversible ion insertion processes [155]. The specific information on the kinetic energy and thermodynamics of the material reactions of solids concerning their structure and composition comes from the electrochemistry technique [155].

The electrical charge can move within solid materials by the lattice macroscopic movement of electronic species or ionic species [156] [157]. Basically, the charge transport is related to electron or ionic motion [156]. Furthermore, the transportation of ionic charge is not required in materials because it causes changes in the properties and qualities of junctions as well as affecting the concentration of the materials and their microstructures [156]. There are several materials that are mixed between ionic and/or electronic conductors [156]-[158]. These mixed conductors are classified as important technologies being used as oxidation and hydrogenation catalysts, chemical separation, fuel cell electrodes, and reactants in microstructure electrodes [156]. Scientists have developed methods to assist the charge transport from separate electronic and ionic components [156]. This method involves the operation of a low amplitude change frequency in the AC measurements, and this procedure is described as impedance spectroscopy to the evaluation of the ionic conductivity of solid electrolytes [156].

In an electrochemical system, the electrodes are described as non-polarizable while the measurements are processed, in ideal conditions [159]. Unless a large voltage drops over the interfaces between the electrolyte and the electrodes, the ideal conditions are eliminated [159].

Otherwise, this problem can be controlled by using separate voltage probes [159]. The reversible electrodes which authorize unimpeded delivery of the mobile ions from one side and their removal on the other side are the most important point for electronic conduction, as long as the ionic conductivity in the electrolyte has a minor electronic conduction, which is determined by the Ohm's law [160]. Experimentally, different ranges of frequencies have been evaluated, such as values from 10^2 Hz to 10^6 Hz, to separate the electrode and the interface-related effects from the electrolyte resulting from the transport processes [160]. Recently, many studies have shown this progress of analysis in experimental data which depends on the frequency of the complex impedance [160]. The ways that we used in our study to analyze and characterize the samples are electrochemical impedance spectroscopy analysis, X-ray diffraction, and scanning electron microscopy.

2.2.1. Electrochemical Impedance Spectroscopy Analysis and The Interfaces Materials ''Grain Boundaries''

Electrochemical impedance spectroscopy (EIS) is an instrument that is widely used in studies of electrochemical systems, for instance, electrolytic cells and batteries [161]. Generally, electrochemical impedance measures the current through the cell by applying an AC potential to the cells; particularly, the electrochemical cells [161] [162]. The EIS technique is applied to know the measurement of the frequency dependence at the impedance of cells, to thus measure the current response by applying a small AC voltage to the cell [161]. The wide use for EIS in fuel cell studies the following points: first, to give microscopic information in the cell system to assist researchers in finding the most appropriate operating conditions and enhance the crystal structure; second, to find the correct modelling of the system with a convenient equivalent circuit and then obtain the electrochemical parameters of the cell system; third, to recognize the

contributions of each component that can assist in identifying if there are problems within cell components; and fourth, to recognize the contributions of the total impedance from the various electrode procedures [163]. EIS is also the common analysis method to analyze the internal processes of electron or ion migration [164] [165]. To analyze these data it is required to measure an extensive frequency range and apply a perfect electrode design to ensure the separation of various polarization operations and analyze the combination impedance data [164].

The impedance spectroscopy has been used in our work to determine the lithium ionic conductivities within the bulk and at the grain boundaries [166]. In brief, electrochemical impedance is the relationship between the responses of the electrochemical cell system and the applied potential [167]. There are three types of electrochemical cells according to the electrode cells as the following: two, three, and four electrode cells, which are used to understand the experiment system of EIS test [167]. Moreover, a two-electrode cell can be used to examine the electrolyte properties from conductivity as an example, or to describe solid-state systems [167]. Three electrode cells are used to examine the applied potential of the electrochemical interface [167]. Four electrode cells are used to measure electrolytes with separation layers, which is a more complex status [167].

In our study, we used an electrochemical analyzer using electrical resistance to analyze and measure the electrical conductivity through two steps. First, the electrode was measured from both sides of the solid sample, which examined the AC impedance plots, and second, the fitting equivalent circuit was obtained, which assisted to investigating the grain boundary resistance and the bulk boundary resistance. To analyze the impedance data results, the most useful technique is the equivalent circuit with ideal models [167]. These equivalent circuit models contain all the data needed for analysis, such as the numbers of the resistor, capacitor,

and inductor to distribute the elements [167]. The equivalent circuit models distribute these elements in a combined way to form complex series and parallel circuits [167]. Generally, using the correct equivalent circuit models is dependent on the data properties, Figure 7 shows these common equivalent circuits, which were designed into Circuit Lab Software and Electrochemical Impedance Spectroscopy Data Analysis Software. These equivalent circuits include some components, one or more of each resistor (R), capacitor (C), and Warburg diffusion element (Z_w). Therefore, as explained in Wang's paper, [167] Figure 7a indicates the simple circuit model to describe the high impedance metal coating, Figure 7b indicates Randel's circuit, which is used to model and describes the oxidation processes and it gives a hint for using more complex equivalent circuits models, at the time the kinetic and diffusion reactions are important, Figure 7c indicates the description of electrode processes, Figure 7d describes the response of batteries, and finally Figure 7e describes the resistance on the metal layer which is in contact with the electrolyte [167].

The value of annealing temperatures cause various conductive results and thus clarify the affection of the impurity phase during high temperatures [168]. This leads to changing the semicircle diameter, as the temperature changes from low to high [168]. Therefore, decreasing the semicircle diameter will boost the Li^+ mobility temperature [168]. As other previous studies reported, they used low-frequency interception on the real impedance axes and the range of 1000 °C for 4 h of centering temperature to obtain total ionic conductivity values of cubic LLZO with Al doped at a range of 1.4×10^{-4} Scm^{-1} to 2.5×10^{-4} Scm^{-1} [21] [82] [132] [153] [156] [169] [170]. Moreover, cubic LLZO with F-doped gave total conductivity 5×10^{-4} Scm^{-1}, which was obtained from a sintered temperature at 1230 ºC / 36 h [45].

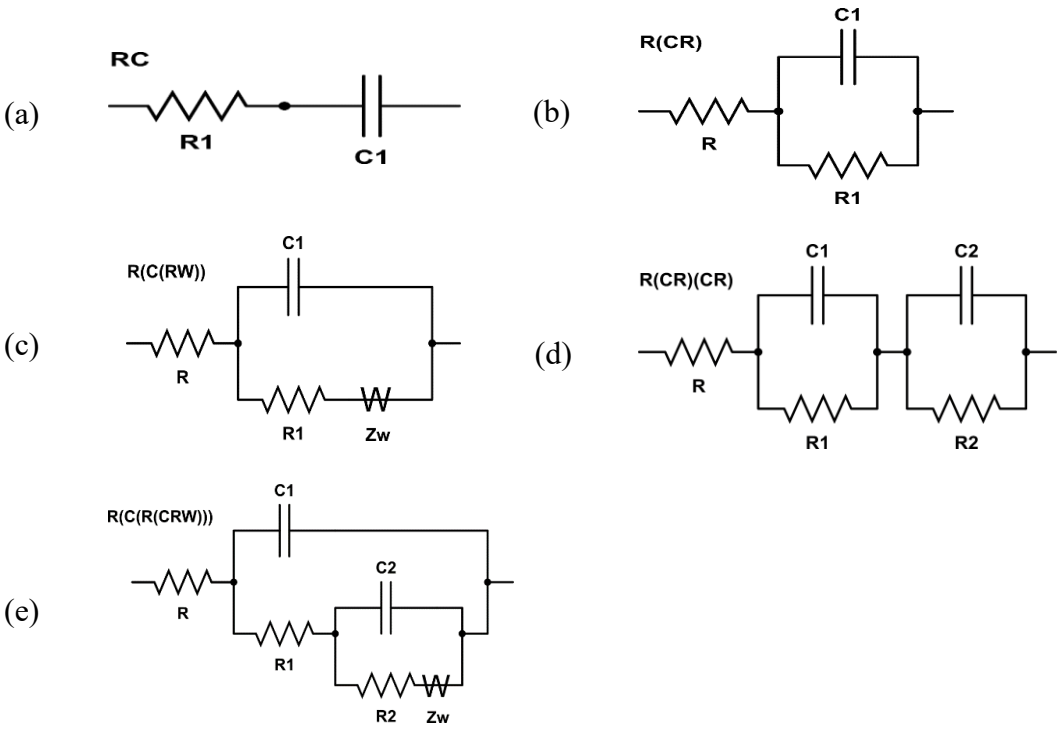

Figure 7. The equivalent circuit design models for electrochemical impedance spectroscopy.

The invention of LLZO and the improvement of Li^+ conductivity that are derived from elemental substitution and cause structural modification of the structure of the atoms were from extensive research efforts [152] [171]-[173]. Researchers have focused on part of the bulk Li^+ conductivity of garnet LLZO to achieve the enhancement from the substitution modification of Li^+ pathway by changing the bulk Li^+ conductivity [21] [32] [145] [173] [174]. The structural discontinuity of grain boundaries, which is also known as grain separation between different phases or different surfaces, presents the interfaces of the materials which are joined with changes in charge transporter concentration [60]. Lithium ionic conductivity can be affected by the net electrostatic charge at the interface and often, there are effects of the grain boundaries on the quality of the conductivity [60] [175].

The concept of increasing the concentration of the mobile species at the interfaces will enhance the ionic conductivity of the materials [60] [177]. In addition, this concept was confirmed by each of the ionic conductivities and activation energy, together with various layer

densities [60] [176]. The relative size influenced by the space charge layer which progressively becomes larger with large densities thus creates a higher concentration and increased ionic conductivity from the charge carriers' influence [60] [176]. In principle and along with interfaces, the present development on nano-sized bulk ion conductors takes a feature of ion conduction [60] [178]. This system of the nano-sized conductors makes the interface of the ion conduction well controlled [60] [175] [176]. It was believed that the presence of the charge at the surface promotes the lithium vacancy diffusion [60] [179].

There are two fundamental processes to optimize Li-ionic conductivity. The first one can be to change the chemical composition by doping and changing the crystal structure or the phase structure. These changes result in more tuning for the Li^+ charge transporter density and mobility along with enhancing the bulk conductivity [164]. The second one is to manage the fabrication process to adjust the ceramic microstructure such as the grain size or grain boundary area to avoid the formation of impurities and secondary phases, which negatively impact the ionic conductivity [164]. Figure 8 shows the sketch of grains and grain boundaries of a LLZO Li^+ conducting ceramic material and an ideal equivalent circuit model. Figure 8a displays the internal bulk grain and grain boundary which contributes to the conductivity of Li^+ conducting ceramic materials [164]. Figure 8b displays the equivalent circuit model with two parallel RC circuits, which represent the interaction between bulk and grain boundary conductivity contributions, and each of the boundary phases are represented as an independent layer of material [164] [166]. As known, the analysis of the impedance spectrum should be modelled based on an equivalent electric circuit consisting of resistor (R) and capacitor (C) components, each one of bulk resistance (R_1), and a bulk capacitor (C_1) obviously shown in Figure 8b describes the internal grain conductive properties and the dielectric properties, respectively,

which are moved by localizing the opposite charges as Li ions and Li vacate [39] [164] [180]. On the other hand, the grain boundary resistance (R_2) and grain boundary capacitor (C_2) represent characteristics of the grain boundaries, where the diffusion of lithium ions is blocked by impurities [164] [181]. As is also known, the polycrystalline materials demonstrate the bulk boundary (inter-grain) and grain boundary impedances which need to be clarified by the same equivalent circuits shown in Figure 8b [39].

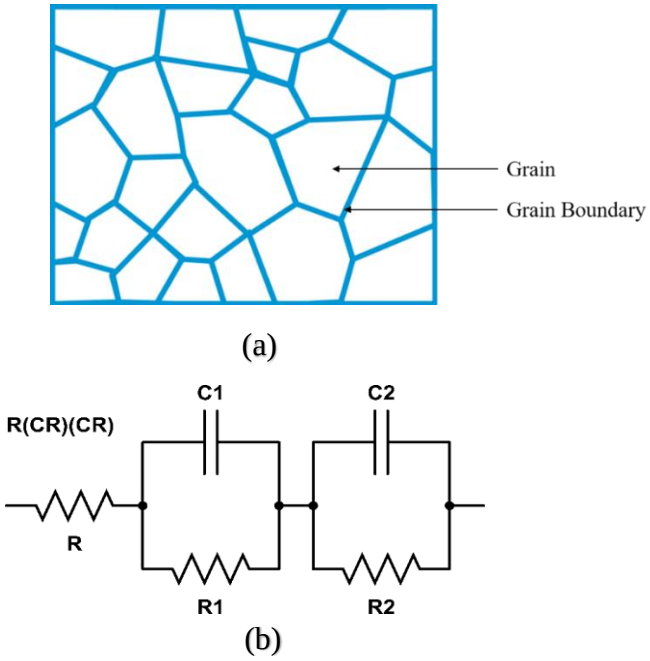

Figure 8. (a) Grains and grains boundaries of LLZO lithium-ion conducting ceramic material (b) equivalent circuit model for bulk and grain-boundary conductivity contributions.

The ideal equivalent circuit in Figure 8b can also be applied to the spectrum in the next figure. Figure 9 shows the Nyquist plot of complex impedance spectrum of two semicircles fitting impedance of AC impedance measured through the LLZO pellets at room temperature. The blue dashed line represents the sample data and the solid red line represents fitted data based on the equivalent circuit model of AC impedance measured through the LLZO pellets. If the semicircle of the grain boundary bracket is large enough, then the bulk bracket will only occur at quite high frequencies above the range of the lab software analysis, thus it will be totally

obscured [173]. It is important to know that the brackets have well-defined intercepts, which result in certain conditions to know the values for R and C; from that, the actual boundary depends on the resistive values, which means the center of the brackets should be separated to stop or avoid the overlapping of the semicircle at the boundaries of the bulk resistance (R_b) + electrode resistance (R_C) intercept [173]. In addition, the capacitances, bulk capacitance (C_b) and grain capacitance (C_g), must be varied by some orders of magnitude [173]. Supposing the Cg and C_b are equal, the brackets will combine into one large bracket [173]. The other important point is the range of frequencies applied [173]. It must be large enough to well define the R_C intercept, although it is difficult to do it experimentally because the frequency range extends to over 5 MHz end with incomplete brackets, or it is possible to lose it completely because of the smaller resistivity of the bulk material, which causes bulk brackets [173].

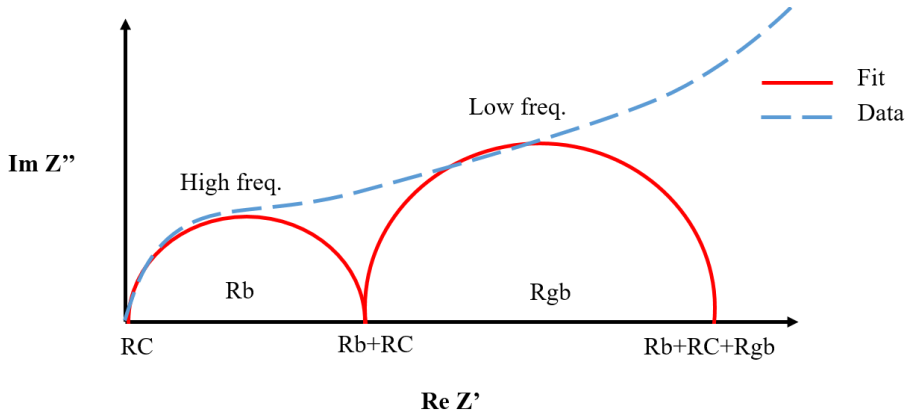

Figure 9. Nyquist plot of the complex impedance of two semicircles’ impedance of AC impedance measuring through the LLZO pellets at room temperature.

Another pattern shown in Figure 10 presents the Nyquist plot from pellets produced from the solid-state reaction powders. Nyquist plots are explained by being fitted with an equivalent circuit model as shown in Figure 10b with the circuit model as one parallel RC circuit, where R and C represent the bulk characteristics of the pattern and R_C is the contact resistance [166]. The values of R and RC can be read directly from the Nyquist plot. R is the value between the

brackets' real intercepts in the x-axis, and RC is the high-frequency intercept [166]. Or the software can be allowed to read it and to get accurate data. Due to the invisibility of the grain-interior bracket, the determination of the grain interior resistance comes from fitting the data and it only determines the grain boundary bracket as shown in Figure 10a [182]. Furthermore, the first RC equivalent circuit is replaced with a single resistor R_1, which is the grain-interior resistance, as shown in Figure 10b [182].

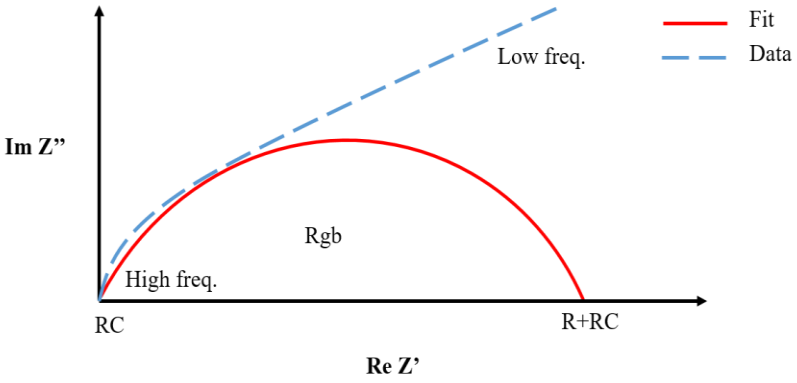

(a)

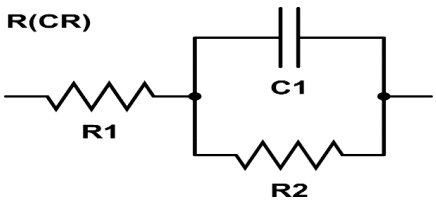

(b)

Figure 10. (a) Nyquist plot of complex impedance of one semicircle and (b) the fit data circuit R_1+C_1‖R_2 of AC impedance measured through the LLZO pellets at room temperature.

A different model of AC impedance spectrum of pellet samples is shown in Figure 11 this shows the Nyquist plot of the impedance spectrum with a two-point blocking electrode in contact with a solid electrolyte [164]. Figure 11a describes the bulk and grain boundary in the Nyquist plot that have absence in their mechanisms, a visible semicircle and the blocking electrodes appear as an ideal of the capacitive behavior [164]. These semicircles are considered

low and the bulk capacitive is not perpendicular to the real part (x-axis) of the plot, and the semicircles model by parallel equivalent circuit of (R-CPE) contains two resistors (R) and three Constant Phase Elements (CPE) as shown in Figure 11b [164]. Sometimes, the collection of circuit components into the model does not yield good fits and the patterns do not show even qualitative similarity with the experimental plots data [183]. However, assuming and adding the distributed components to the circuit, such as CPE, has been a suitable method [183] [184]. Typically, there are two distinct features of the impedance spectra of ionic conducting ceramic demonstrations, which are the bulk and grain boundary impedance and typical capacitances [185]. Due to that, the semicircle will not completely appear in the impedance spectra; nevertheless, the data will fit the semicircle which is related to the grain boundary well [185].

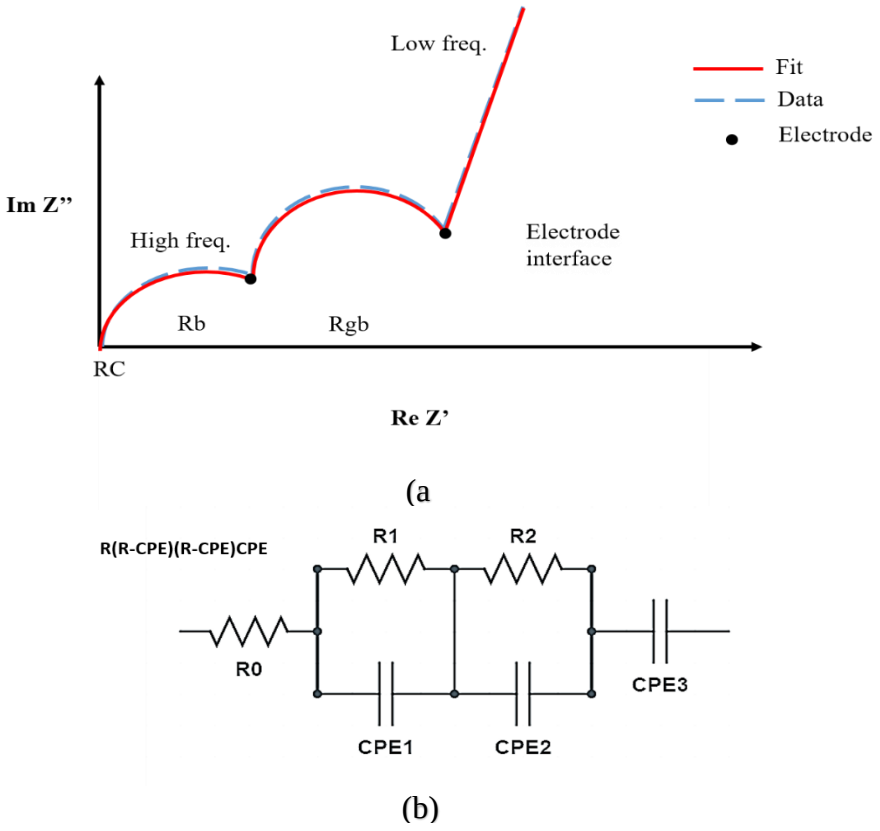

Figure 11. (a) The Nyquist plot of complex impedance with two different frequencies of semicircle impedance, (b) the ideal fitting circuit $R_0+R_1\|CPE_1+R_2\|CPE_2+CPE_3$ of AC impedance measured through the LLZO pellets at room temperature.

Figure 12 displays a Nyquist plot of the complex impedance with one semicircle impedance and a long frequency tail of an electrode interface of AC impedance measured through the LLZO pellets at room temperature. Fitting this impedance spectrum is convenient for the equivalent circuit, which includes two RC circles, like in the equivalent circuit shown in Figure 11b [186].

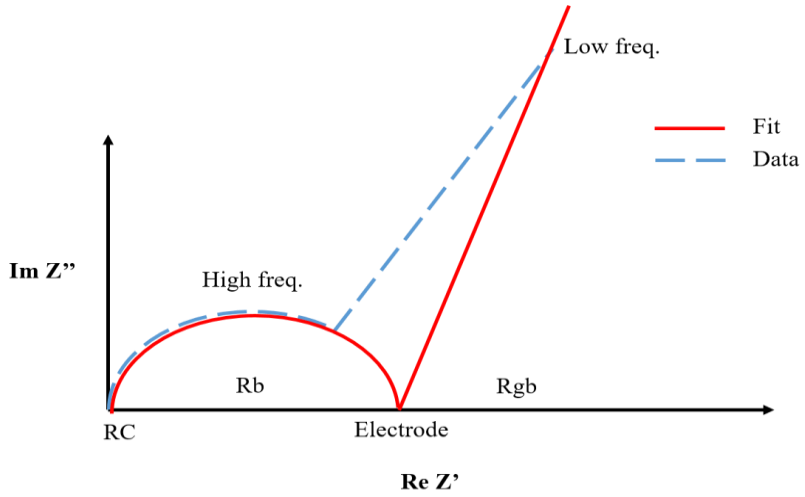

Figure 12. The Nyquist plot of complex impedance with one semicircle impedance and long frequency tail of electrode interface of AC impedance measured through the LLZO pellets at room temperature.

The other case is when there is no semicircle of bulk impedance that can be observed except for the turning point at the high-frequency region, which is observed in some dope materials of LLZO, such as F-doped LLZO [45]. Figure 13 shows the Nyquist plot of impedance with no semicircle of bulk resistance. The electrode resistance is reflected as a small tail at the low-frequency region, which indicates that the electrode blocks mobile lithium ions [45]. It is known that the semicircle in Nyquist plot arises from the bulk boundary and grain-boundary resistance; however, Figure 13 implied that the small tail of the grain-boundary resistance might be negligible compared to the bulk resistance [45]. This means Li^+ is blocked at the electrode and reveals the material to be considered as Li^+ conductor [157] [187]. However, the value of the grain boundary resistance can be read directly from the real part (Z', x-axis) as the arrow marks

on the Nyquist plot with grey color. The ideal semicircle model to fit the data here is the same as what is shown in Figure 11b with R_0+R_1‖CPE_1+R_2‖CPE_2+CPE_3.

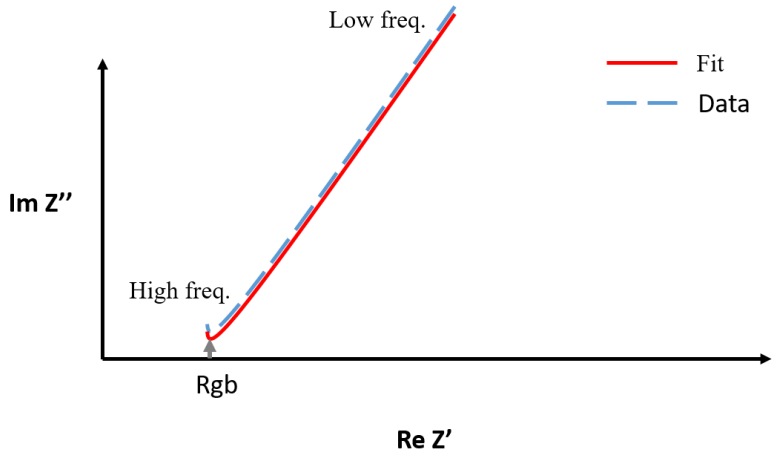

Figure 13. The Nyquist plot of impedance with no semicircle of bulk resistance of AC impedance measured through the LLZO pellets at room temperature.

The analyzer/workstation was designed to measure different parameters, for instance, the real and imaginary parts of the impedance, admittance, permittivity, modulus, and capacitance together with a specific frequency (0.1 Hz to 1 MHz) at room temperature [188]. The model of the equivalent circuit we selected for our samples is as shown in Figure 11b. The analyzer/workstation was controlled by the Electrochemical Instrumentation (CH 650E), EC-Lab software, version: 10.40 (demo), and ZSimpWin Electrochemical Impedance Spectroscopy analysis software, version 1.0.0 (demo) to view and fit the output data to ideal circuit models.

2.2.2. X-Ray Powder Diffraction

The technique of X-ray Powder Diffraction (XRD) is a quick analytical process for phase identification that analyzes crystalline structure material and the width of the diffraction peaks [167] [189]. In addition, it gives information regarding the XRD pattern, the parameters of the lattice, crystallite size from the position of the crystals, and peak intensity, and can provide data on unit cell dimensions [167] [189]. In brief, the identification of the crystal phase and the unit cell dimensions are the main objects of using the XRD technique; thus, this technique works by

hitting the sample with a photon source and then calculating the deductive wave as a result [167]. The basic mechanism of XRD is described as follows. First, the XRD uses electromagnetic radiation that has a similar number of the distance between atoms which is related to a wavelength between 0.01 to 10 nanometres (nm) [167]. Second, every atom contains electrons with various numbers that are able to scatter light, and these atoms in the crystal structure unit cell are coordinated in a periodic order, which forms many diffracting planes [167]. The atoms are coordinated in a different way in the unit cell; hence it is understood that in various crystal materials, the unit cells also vary [167].

Many papers have reported the diffraction process from using both X-rays and neutrons, which determine the crystal structures of Li garnets [77] [97] [99] [119] [126] [138] [139] [159] [190]-[192]. The component of Li garnets causes problems during the experiments with the diffraction process [119]. The poor scattering of the Li powder-based structure component makes it the main problem during the application of the X-ray diffraction and determining atomic displacement parameters [119]. The importance of knowing a quantitative determination of Li site occupancy which depends on correct measurement which is very necessary to recognize the diffusion behavior; however, the measurements are still limited by using the neutron powder diffraction measurements, and it is much sensitive at detecting the Li garnet atom [119]. Presently, with this issue, which is related to describing the Li atoms correctly, there are some crystal diffraction measurements with more data groups on Li garnets, which also have problems regarding describing the atoms correctly as the neutron measurements [99] [119] [193].

In our study, we used the X-ray diffraction XRD of (Bruker D8 AXS, XRD diffractometer, Cu Kα radiation) to characterize the LLZO powder after the annealing at 1230 ºC for 8 h. The measurement was conducted in the range from 10º to 70º of 2θ at a step of 0.02 º/s.

2.2.3. Scanning Electron Microscopy and Energy Dispersive X-Ray Spectroscopy

The techniques of Scanning Electron Microscopy (SEM) and Energy Dispersive X-ray Spectroscopy (EDS) have the potential to establish and introduce the major information on the material composition of scanned specimens [194]. SEM is an effective method to analyze materials such as solid inorganic materials and organic including polymers [194]. SEM and EDS can provide information, results, and images both qualitatively and semi-quantitatively [194]. SEM can provide data on crystalline structure, surface topography, chemical composition, and electrical attitude of the specimen scale of a nanometer (nm) to micrometer (μm) size [194] [195].

In our study, we used the Scanning Electron Microscopy (SEM) and Energy Dispersive X-ray Spectroscopy (EDS) to analyze the LLZO pellets after annealed at 1230 ºC in terms of the morphology, microstructure, and composition.

CHAPTER 3. RESULTS AND DISCUSSION

3.1. Crystal Structure and Phase Analysis

Figure 14 shows the XRD spectrum of $Li_7La_3Zr_2O_{12}$ (x = 1.768) calcined material, which clearly shows one phase of tetragonal structure. The crystallinity and intensities in the diffraction peaks of LLZO show tetragonal structure crystallinity. The impurity of the tetragonal-LLZO produced a lot of noticeable peaks on the spectrum. That reveals and belongs to the insignificant formation of the secondary phases in Li_2ZrO_3. Two different peaks are revealed here. One is the peak at 18º. Second are the overlapping peaks at 29º and 52º. These peaks for each of secondary phases of $La_2Zr_2O_7$ may be caused by the excess lithium, which was used to avoid lithium loss during the annealing process. The tetragonal phase of LLZO is assured with splitting peaks in the range between 18º to 60º at 2 theta. However, the cubic phase confirms the absence of splitting in the peaks, which is absent on our spectra.

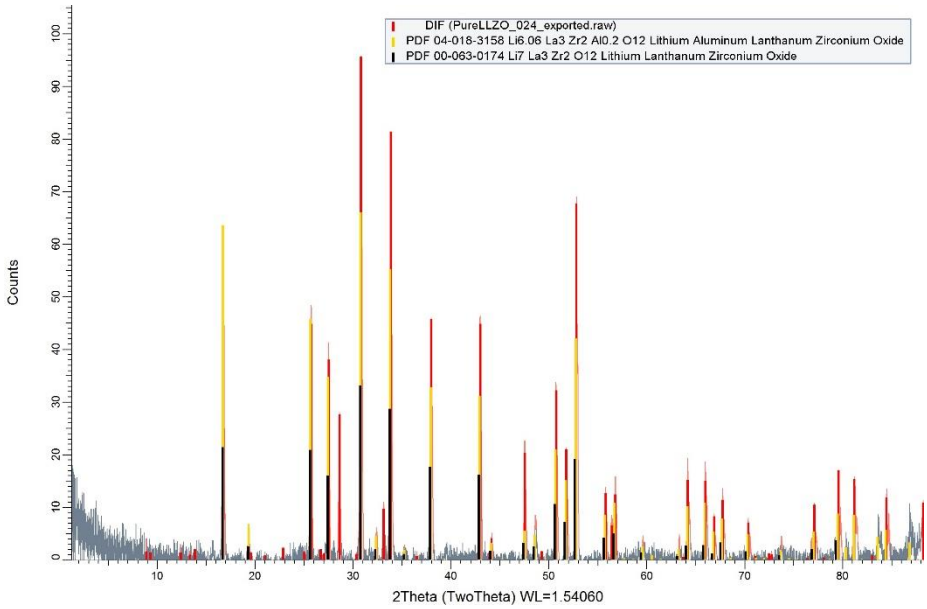

Figure 14. The XRD pattern of the complex composition of $Li_7La_3Zr_2O_{12}$ annealed at 1230 °C and measured at room temperature.

3.2. Microstructure Analysis

Figure 15 shows the SEM images of LLZO sample synthesized at 1230 ºC for 8 h, which was carefully polished at room temperature to reduce differences caused by surface roughness. As our results show, the grain size is more than 1 μm, and the correlation between grains is very poor in Figure 15a; moreover, some of grains are correlated by grain boundaries and it revels the short path for the conduction of Li^+, as shown in Figure 15b.

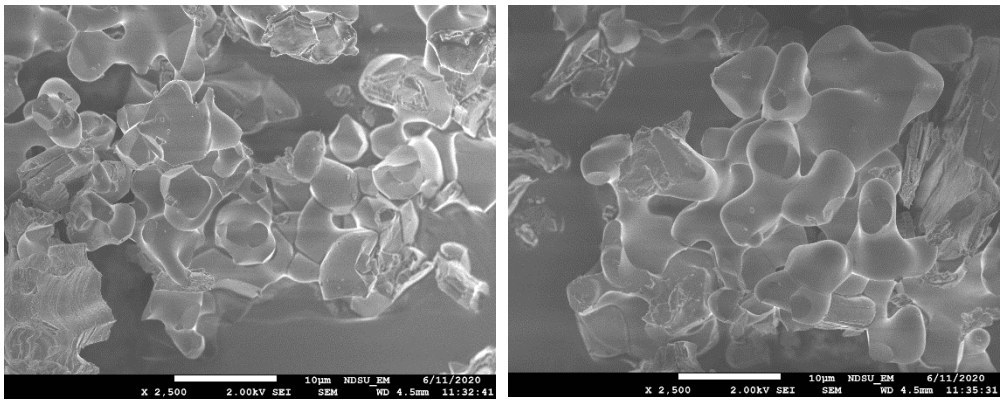

(a) (b)

Figure 15. (a) and (b) The SEM images of the calcination pellets at 1230 ºC.

Figure 16 displays the EDS chart of element behavior of the $Li_7La_3Zr_2O_{12}$ sample at 1230 ºC for each O_2, La_2O_3 and ZrO_2. As one can see, these elements have different peaks in both Figure 16a and Figure 16b that use two different scales and integral counts. These values were throughout the surface of the pellet. The stoichiometric atomic ratio is shown in Table 2 with two measure scales: 992-53850 and 2160-108290, respectively. These elements are distributed and the Al component may come from the alumina crucible during the annealing step. In addition, the absence of the Li component in the atomic ratio table is because the incapability of SEM in detecting the Li element with the low energy radiation.

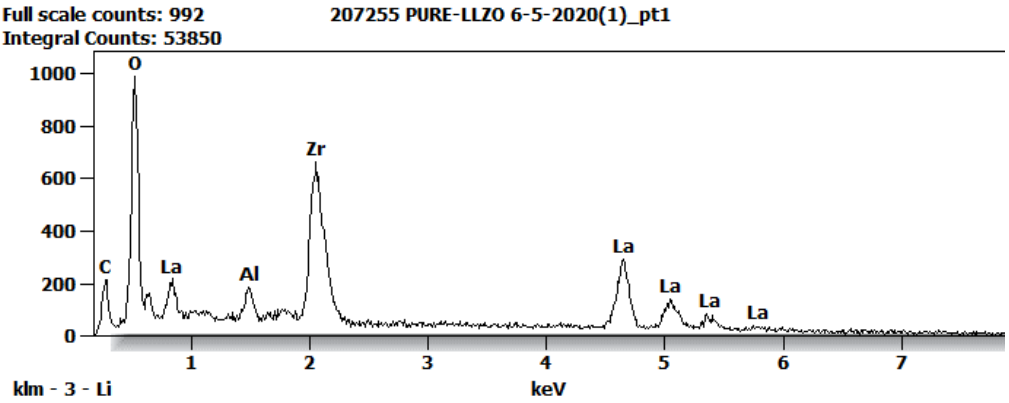

(a)

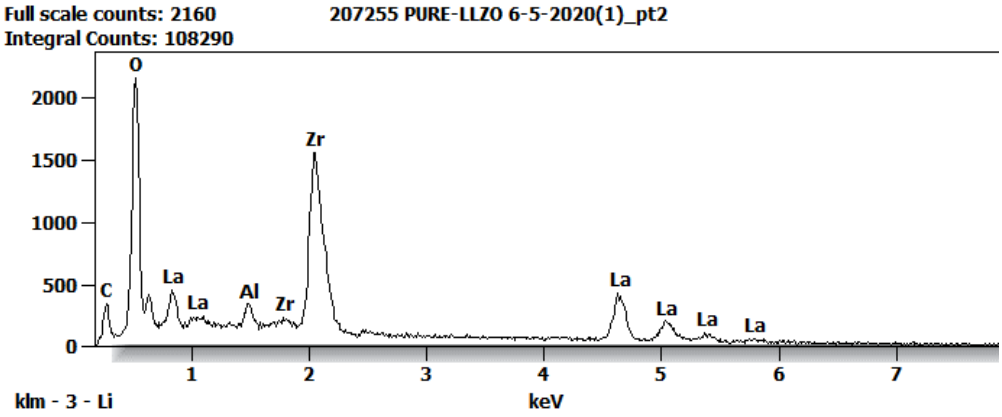

(b)

Figure 16. The EDS of element chart of an $Li_7La_3Zr_2O_{12}$ pellet annealed at 1230 ºC using different scales and integral counts (a) 992-53850 and (b) 2160-108290, respectively.

Table 2. The atomic ratio of $Li_7La_3Zr_2O_{12}$ sample based on Figure 16.

Sample / scales and integrals count	C	O	Al	Zr	La
LLZO / 992-53850	8.22	53.65	3.17	16.46	18.51
LLZO / 2160-108290	6.35	61.28	2.03	17.76	12.51

3.3. AC Impedance Spectroscopy of LLZO

The Nyquist plot of LLZO pellets pressed manually and annealed at 1230 ºC and measured at room temperature shown in Figure 17. The Nyquist plots of the impedance spectra measured in air at room temperature of eight samples and eight formulas as shown in Table 3.

Table 3. Samples and formulas of LLZO pellets based on Nyquist plots of the impedance spectra in Figure 17 measured in air at room temperature.

Sample	Formula
Pure-LLZO	$Li_7La_3Zr_2O_{12}$
Al-LLZO	$Li_7Al_{0.2}La_3Zr_2O_{12}$
F-LLZO	$Li_7La_3Zr_2O_{12}F_2$
Ta-LLZO	$Li_{6.4}La_3Zr_{1.4}Ta_{0.6}O_{12}$
Ta, F-LLZO	$Li_{6.7}La_3Zr_{1.7}Ta_{0.3}O_{11.5}F_{0.5}$
Al and F-LLZO	$Li_{6.7}Al_{0.1}La_3Zr_2O_{11.5}F_1$
Al and Ta-LLZO	$Li_{6.4}Al_{0.1}La_3Zr_{1.7}Ta_{0.3}O_{12}$
Al and Ta and F-LLZO	$Li_{6.6}Al_{0.06}La_3Zr_{1.8}Ta_{0.2}O_{11.67}F_{0.67}$

The AC impedance conductivity of the results of both cubic and tetragonal LLZO is shown in Figure 17. There are some remarkable points shown and noticed in Figure 17. Any obvious semicircles cannot be observed for all curves except for Ta-doped LLZO. The only thing that can be noticed is the low frequency tail that is almost upright with the impedance line of the imaginary part (Z'', y-axes). This tail references a particular ionic conductor that comes from using the Li^+ blocking electrodes. In this case, to connect the high frequency with grain boundary impedance, we found that using the high frequency ~1×10^6 Hz, leads reach high Li^+ conductivity.

Since the samples were almost dense; we understand that for cubic LLZO the lattice conductivity and the grain boundary are identical in terms of magnitude. This appeared just in part of the conductivity data of all these samples $Li_7La_3Zr_2O_{12}$, $Li_7Al_{0.2}La_3Zr_2O_{12}$, $Li_7La_3Zr_2O_{12}F_2$, $Li_{6.7}La_3Zr_{1.7}Ta_{0.3}O_{11.5}F_{0.5}$, $Li_{6.7}Al_{0.1}La_3Zr_2O_{11.5}F_1$, $Li_{6.4}Al_{0.1}La_3Zr_{1.7}Ta_{0.3}O_{12}$ and $Li_{6.6}Al_{0.06}La_3Zr_{1.8}Ta_{0.2}O_{11.67}F_{0.67}$; however, the other sample $Li_{6.4}La_3Zr_{1.4}Ta_{0.6}O_{12}$ appeared to be tetragonal phase LLZO as the conductivity data showed, despite the application of the activation dopant process.

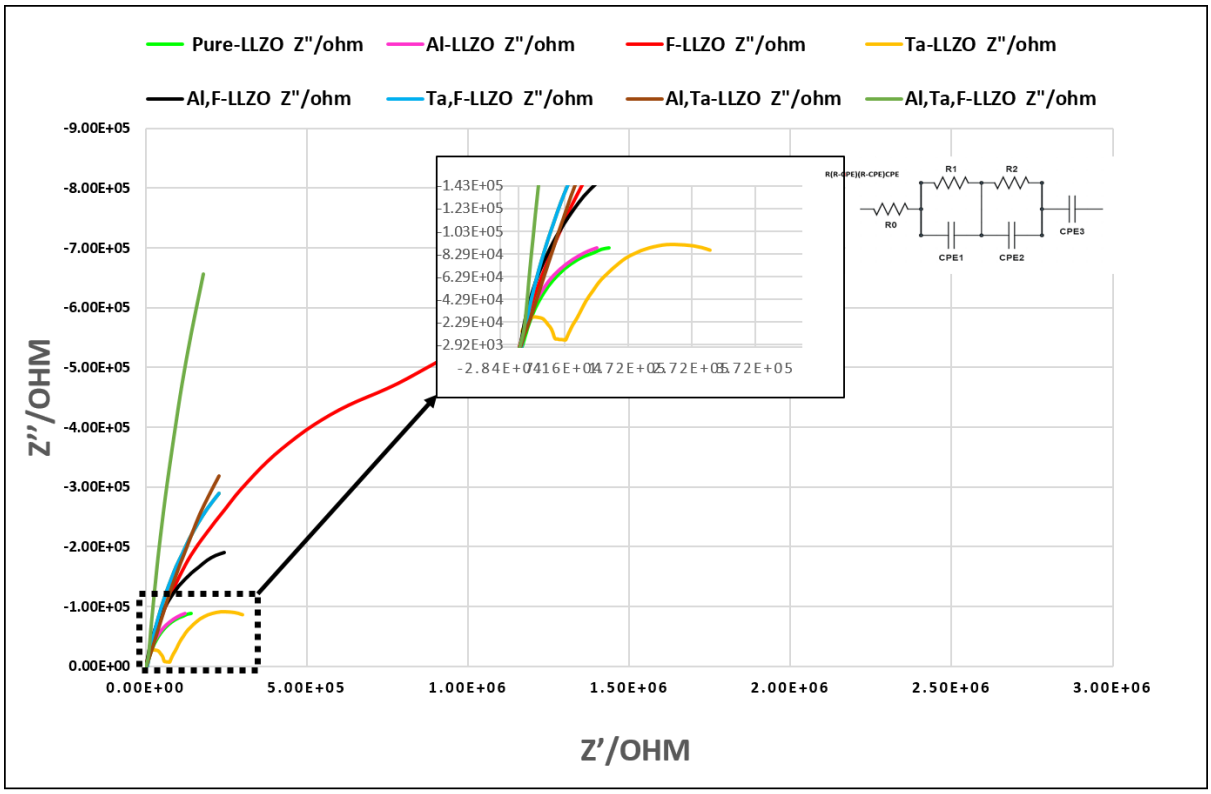

Figure 17. The impedance spectra plot of pure LLZO, Al-LLZO, F-LLZO, Ta-LLZO, co-doped Al and F-LLZO, Ta and F-LLZO, Al and Ta-LLZO, and multi-doped Al and Ta and F-LLZO respectively, (1-10^6 Hz) at room temperature.

The Li^+ conductivity of the pellets of the LLZO solid-state electrolyte was measured using the EIS method. In general, this method uses two electrodes of Ti films coated on the two sides of pellet samples. In addition, to complete this process, the EIS result curves should have bulk resistance and grain boundary resistance, (note that grain boundary resistance could be absent in some cases) which was shown clearly on the connecting computer screen, and EIS should fit these results with an appropriate equivalent circuit as shown in Figure 11b, the ideal fitting circuit we used was $R_0(R_1\text{-}CPE_1)(R_2\text{-}CPE_2)CPE_3$ of AC impedance measured through the LLZO pellets at room temperature by using Randomize + Simplex method. The exact impedance fitting of samples curves were shown in Appendix Figures A1-A8 for samples of LLZO, Al-LLZO, F-LLZO, Ta-LLZO, co-doped Al and F-LLZO, Ta and F-LLZO, Al and Ta-LLZO, and

multi-doped Al and Ta and F-LLZO respectively. The conductivity is calculated using equation 1. It comes after applying equation 2, the sum of each bulk resistance R_b and grain boundary resistance R_{gb} where R_t refers to the total resistance, R_b is the bulk resistance, and R_{gb} is the grain boundary resistance.

$$R_t = R_b + R_{gb} \quad \text{(Eq. 2)}$$

The conductivity values with all of these eight different sample components are described as two parts. The first is the general part, which presents the best ionic conductivity results, as Figure 18 shows the conductivity values for these components: Pure-LLZO, Al-LLZO, F-LLZO, Ta-LLZO, co-doped Ta and F-LLZO, Al and F-LLZO, Al and Ta-LLZO, and multi-doped Al and Ta and F-LLZO, respectively. These values are 4.81×10^{-5} Scm^{-1}, 4.81×10^{-5} Scm^{-1}, 5.90×10^{-5} Scm^{-1}, 3.48×10^{-6} Scm^{-1}, 1.40×10^{-4} Scm^{-1}, 8.14×10^{-5} Scm^{-1}, 1.20×10^{-4} Scm^{-1}, and 1.67×10^{-4} Scm^{-1}, respectively, at room temperature and after annealing at 1230 ºC. Moreover, the highest conductivity present with multi-doped Al and Ta and F-LLZO was ~1.67×10^{-4} Scm^{-1}, thereafter was the co-doped Ta and F-LLZO was ~1.40×10^{-4} Scm^{-1}, then the co-doped Al and Ta-LLZO was ~1.20×10^{-4} Scm^{-1}. Also, the other five components were: pure LLZO, Al-LLZO, F-LLZO, Ta-LLZO, co-doped Al and F-LLZO, which are clearly listed in Table 4. As a result, we can demonstrate that the multi-doped on the Li site with the Al element, Zr site with the Ta element, and the O site with the F element of $Li_{6.6}Al_{0.06}La_3Zr_{1.8}Ta_{0.2}O_{11.67}F_{0.67}$ gave the highest ionic conductivity, which means low defect/impurity concentration of the phase structure. Figure 19 displays the error bar results for these eight samples' conductivity data. There are three colored lines on the plot the red line to introduce the maximum (Max) conductivity, the yellow line to introduce the average (Avg) conductivity, and the green line to introduce the minimum (Min) conductivity.

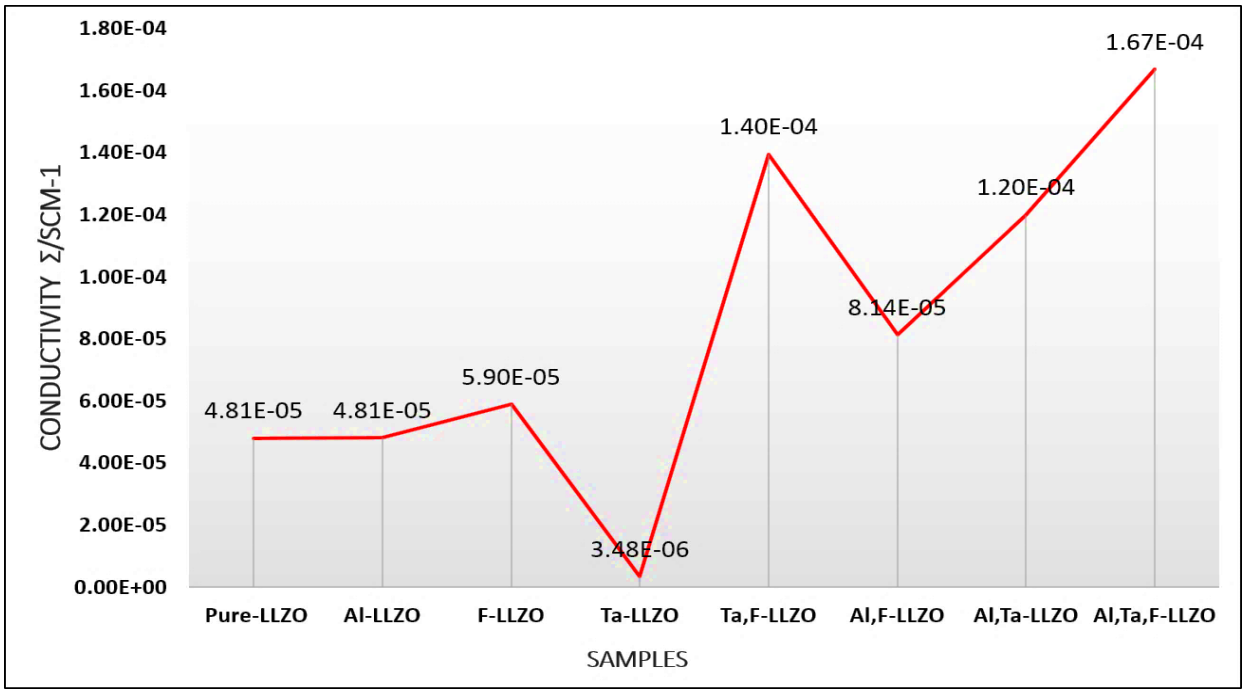

Figure 18. The best (Max) results for pure LLZO, co-doped LLZO, and multi-doped LLZO at room temperature.

Table 4. Summary of ionic conductivity with other data of the tested samples at room temperature.

Sample	σ/Scm^{-1} at RT	Rb /Ω	Rg /Ω	Rgb /Ω
LLZO	4.81×10^{-5}	7.89×10^{2}	3.19×10^{3}	3.98×10^{3}
Al-LLZO	4.81×10^{-5}	6.18×10	3.92×10^{3}	3.98×10^{3}
F-LLZO	5.90×10^{-5}	2.89×10^{2}	3.33×10^{5}	3.34×10^{5}
Ta-LLZO	3.48×10^{-6}	4.88×10^{3}	5.04×10^{4}	5.53×10^{4}
Ta and F-LLZO	1.40×10^{-4}	7.54×10^{2}	1.10×10^{3}	1.85×10^{3}
Al and F-LLZO	8.14×10^{-5}	9.98×10^{2}	2.17×10^{3}	3.17×10^{3}
Al and Ta-LLZO	1.20×10^{-4}	7.84×10^{2}	1.43×10^{3}	2.21×10^{3}
Al and Ta and F-LLZO	1.67×10^{-4}	1.03×10^{3}	5.79×10^{3}	6.82×10^{3}

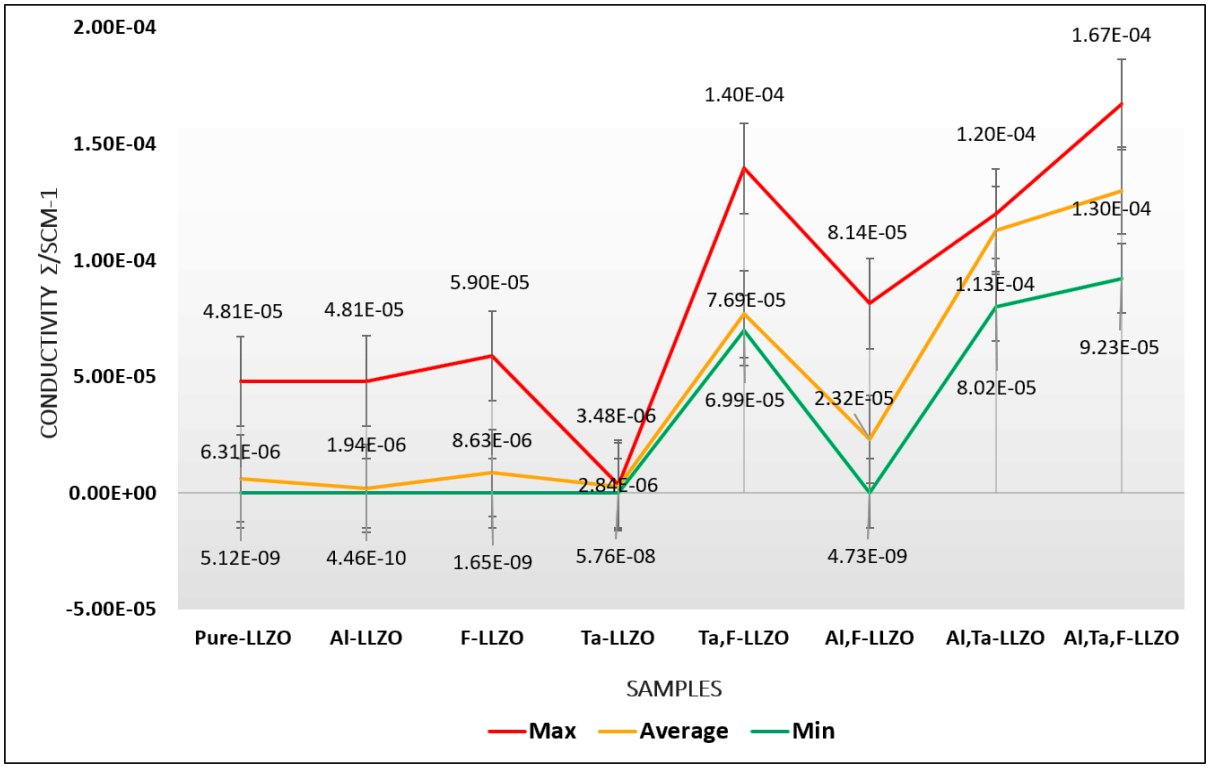

Figure 19. The Error Bar results of the maximum (red line), average (yellow line), and minimum (green line) conductivities data of Pure-LLZO, Al-LLZO, F-LLZO, co-doped Al and F-LLZO, and multi-doped Al and Ta and F-LLZO at room temperature.

The second is the specific part, which presents different conductivity data with different concentrations of the amount of the materials. In the single doped Al-LLZO, with two different concentration groups, group 1 includes changing the amount of Li_2CO_3 and Al in each of 5 formulas and group 2 includes changing only the amount of Al in each of 5 formulas, as shown in Table 5. By comparing these data of Al-doped LLZO with the previous data which used the same formula $Li_{6.7}Al_{0.1}La_3Zr_2O_{12}$ and under the same conditions, it can be noticed that the only difference was the Li type. Group 1 and 2 used Li_2CO_3 which gave $\sigma \sim 1.01\times10^{-6}$ Scm^{-1} at room temperature as the highest data; on the other hand, the same formula was repeated with LiOH which gave $\sigma \sim 4.81\times10^{-5}$ Scm^{-1} at room temperature with the same procedures and conditions. A little more Li_2CO_3 and Al were added as the formula $Li_7Al_{0.2}La_3Zr_2O_{12}$ in group 2, gave $\sigma \sim 3.09\times10^{-5}$ Scm^{-1} at room temperature, thus, Li_2CO_3 was gave an approximate value from using

LiOH. From that, to our knowledge, we considered that the mechanisms and effects of each Li (LiOH) or (Li_2CO_3) component and the quantity of Al component concentration should be taken it seriously. Therefore, the associated air exposure (O_2 and/or CO_2) and the humid air (O_2 and H_2O) could affect the interfacial impedance, which was evident from the results of the conductivity. In addition, as we know an increase in Al component concentration gave lower conductivity due to the contamination with the aluminum crucible, which cause the pellet sample to be affected by a quantity of Al concentration and Al_2O_3 crucible, as Table 3 shows. On the other hand, co-doped Al and F-LLZO, with the formula ($Li_{6.7}Al_{0.1}La_3Zr_2O_{11.5}F_{0.1}$) which F = 0.1 mole, gave ionic conductivity $\sigma \sim 1.60\times10^{-4}$ Scm^{-1} at room temperature. Comparing this with the same formula $Li_{6.7}Al_{0.1}La_3Zr_2O_{11.5}F_1$ but with different amount of F = 1 mole, giving higher ionic conductivity $\sigma \sim 8.14\times10^{-5}$ Scm^{-1} at room temperature as Table 4 previously showed, we noticed that increasing the amount of F can give lower result data; however, if the concentration of Al is 0.2 mole or above and F is 2 moles or above, the conductivity dropped to a lower level as we noticed with the sample formula $Li_{6.4}Al_{0.2}La_3Zr_2O_{11}F_2$ which gave $\sigma \sim 5.37\times10^{-7}$ Scm^{-1} at room temperature. Thus, studying these specifics made us gain a better understanding of the general and specific impacts of each material.

Table 5. Summary of the ionic conductivity Al-LLZO and the concentration amount of formulas in two groups of the tested samples at room temperature.

Samples group 1	σ/Scm^{-1} at RT	Samples group 2	σ/Scm^{-1} at RT
$Li_{6.7}Al_{0.1}La_3Zr_2O_{12}$	1.01×10^{-6}	$Li_7Al_{0.1}La_3Zr_2O_{12}$	5.10×10^{-7}
$Li_{6.4}Al_{0.2}La_3Zr_2O_{12}$	5.60×10^{-7}	$Li_7Al_{0.2}La_3Zr_2O_{12}$	3.09×10^{-5}
$Li_{6.1}Al_{0.3}La_3Zr_2O_{12}$	5.84×10^{-7}	$Li_7Al_{0.3}La_3Zr_2O_{12}$	1.28×10^{-6}
$Li_{5.8}Al_{0.4}La_3Zr_2O_{12}$	9.67×10^{-8}	$Li_7Al_{0.4}La_3Zr_2O_{12}$	1.87×10^{-6}
$Li_{5.5}Al_{0.5}La3Zr_2O_{12}$	6.09×10^{-8}	$Li_7Al_{0.5}La3Zr_2O_{12}$	1.42×10^{-6}

CHAPTER 4. CONCLUSION AND FUTURE PROSPECTIVE

The garnet-type of $Li_7La_3Zr_2O_{12}$ (LLZO) solid-state electrolyte was successfully synthesized and achieved by using a solid-state reaction method based process involving sintering at 1230 ºC for 8 hours. The stabilization of the LLZO substance come from selecting specific types of dopants and adopting combined doping. The optimization of the material combination leads to a significant and impressive increase in the lithium ionic conductivity of LLZO. The best total ionic conductivity was achieved with the multi-doped LLZO with Al and Ta and F ~1.67×10^{-4} Scm^{-1} to stabilize the structure. Therefore, this highest lithium-ion conductivity makes this compound have its own distinct characteristics, safe and clean material, and its assembly is also an evidence of a promising high efficiency battery that will serve human lives and lead the community to have a better energy source. In a future perspective, the conditions of sintering temperatures and dopant ratio processes can be modified to get higher lithium-ion conductivity and operate the battery with a spreadable interlayer that could produce more stability and improve density for the solid-state batteries.

REFERENCES

[1] S. Ramakumar, C. Deviannapoorani, L. Dhivya, L. S. Shankar, and R. Murugan, “Lithium garnets: Synthesis, structure, Li+ conductivity, Li+ dynamics and applications,” Prog. Mater. Sci., vol. 88, pp. 325–411, 2017, doi: 10.1016/j.pmatsci.2017.04.007.

[2] M. S. Whittingham, “History, evolution, and future status of energy storage,” Proc. IEEE, vol. 100, no. SPL CONTENT, pp. 1518–1534, 2012, doi: 10.1109/JPROC.2012.2190170.

[3] S. Fletcher, Bottled lightning: superbatteries, electric cars, and the new lithium economy. Hill and Wang, 2011.

[4] K. H. LaCommare and J. H. Eto, “Understanding the cost of power interruptions to US electricity consumers,” Lawrence Berkeley National Lab.(LBNL), Berkeley, CA (United States), 2004.

[5] L. E. Friesen, “No evidence of large-scale fatality events at Ontario wind power projects,” vol. 29, no. 3, pp. 149–156, 2011.

[6] S. Yan et al., “Research Advances of Amorphous Metal Oxides in Electrochemical Energy Storage and Conversion,” Small, vol. 15, no. 4, pp. 1–30, 2019, doi: 10.1002/smll.201804371.

[7] B. Dunn, H. Kamath, and J. M. Tarascon, “Electrical energy storage for the grid: A battery of choices,” Science (80-.)., vol. 334, no. 6058, pp. 928–935, 2011, doi: 10.1126/science.1212741.

[8] T. S. Mathis, N. Kurra, X. Wang, D. Pinto, P. Simon, and Y. Gogotsi, “Energy Storage Data Reporting in Perspective—Guidelines for Interpreting the Performance of Electrochemical Energy Storage Systems,” Adv. Energy Mater., vol. 9, no. 39, pp. 1–13, 2019, doi: 10.1002/aenm.201902007.

[9] Z. Yang et al., “Electrochemical energy storage for green grid,” Chem. Rev., vol. 111, no. 5, pp. 3577–3613, 2011, doi: 10.1021/cr100290v.

[10] M. Yang, Y. Zhong, J. Ren, X. Zhou, J. Wei, and Z. Zhou, “Fabrication of High-Power Li-Ion Hybrid Supercapacitors by Enhancing the Exterior Surface Charge Storage,” Adv. Energy Mater., vol. 5, no. 17, pp. 1–7, 2015, doi: 10.1002/aenm.201500550.

[11] M. J. Uddin and S. J. Cho, “Reassessing the bulk ionic conductivity of solid-state electrolytes,” Sustain. Energy Fuels, vol. 2, no. 7, pp. 1458–1462, 2018, doi: 10.1039/c8se00139a.

[12] J. B. Goodenough and K. S. Park, “The Li-ion rechargeable battery: A perspective,” J. Am. Chem. Soc., vol. 135, no. 4, pp. 1167–1176, 2013, doi: 10.1021/ja3091438.

[13] J. M. Tarascon and M. Armand, “Issues and challenges facing rechargeable lithium batteries,” Mater. Sustain. Energy A Collect. Peer-Reviewed Res. Rev. Artic. from Nat. Publ. Gr., vol. 414, no. November, pp. 171–179, 2010, doi: 10.1142/9789814317665_0024.

[14] B. Scrosati, J. Hassoun, and Y. K. Sun, “Lithium-ion batteries. A look into the future,” Energy Environ. Sci., vol. 4, no. 9, pp. 3287–3295, 2011, doi: 10.1039/c1ee01388b.

[15] K. Mizushima, P. C. Jones, P. J. Wiseman, and J. B. Goodenough, “LixCoO2 (0<x≤1): A new cathode material for batteries of high energy density,” Solid State Ionics, vol. 3–4, no. C, pp. 171–174, 1981, doi: 10.1016/0167-2738(81)90077-1.

[16] W. D. Richards, L. J. Miara, Y. Wang, J. C. Kim, and G. Ceder, “Interface Stability in Solid-State Batteries,” Chem. Mater., vol. 28, no. 1, pp. 266–273, 2016, doi: 10.1021/acs.chemmater.5b04082.

[17] H.-P. Hong, “Crystal structure and ionic conductivity of Li14Zn (GeO4) 4 and other new Li+ superionic conductors,” Mater. Res. Bull., vol. 13, no. 2, pp. 117–124, 1978.

[18] D. Fauteux and R. Koksbang, “Rechargeable lithium battery anodes: alternatives to metallic lithium,” J. Appl. Electrochem., vol. 23, no. 1, pp. 1–10, 1993.

[19] K. Takada, “Progress and prospective of solid-state lithium batteries,” Acta Mater., vol. 61, no. 3, pp. 759–770, 2013, doi: 10.1016/j.actamat.2012.10.034.

[20] J. F. M. Oudenhoven, L. Baggetto, and P. H. L. Notten, “All-solid-state lithium-ion microbatteries: A review of various three-dimensional concepts,” Adv. Energy Mater., vol. 1, no. 1, pp. 10–33, 2011, doi: 10.1002/aenm.201000002.

[21] S. Ohta, T. Kobayashi, and T. Asaoka, “High lithium ionic conductivity in the garnet-type oxide Li7-X La3(Zr2-X, NbX)O12 (X = 0-2),” J. Power Sources, vol. 196, no. 6, pp. 3342–3345, 2011, doi: 10.1016/j.jpowsour.2010.11.089.

[22] A. Dumon, M. Huang, Y. Shen, and C. W. Nan, “High Li ion conductivity in strontium doped Li7La 3Zr2O12 garnet,” Solid State Ionics, vol. 243, pp. 36–41, 2013, doi: 10.1016/j.ssi.2013.04.016.

[23] S. Chen, K. Wen, J. Fan, Y. Bando, and D. Golberg, “Progress and future prospects of high-voltage and high-safety electrolytes in advanced lithium batteries: from liquid to solid electrolytes,” J. Mater. Chem. A, vol. 6, no. 25, pp. 11631–11663, 2018.

[24] A. J. Samson, K. Hofstetter, S. Bag, and V. Thangadurai, “A bird’s-eye view of Li-stuffed garnet-type Li 7 La 3 Zr 2 O 12 ceramic electrolytes for advanced all-solid-state Li batteries,” Energy Environ. Sci., vol. 12, no. 10, pp. 2957–2975, 2019.

[25] V. Thangadurai and W. Weppner, “Li6ALa2Ta2O12 (A=Sr, Ba): Novel garnet-like oxides for fast lithium ion conduction,” Adv. Funct. Mater., vol. 15, no. 1, pp. 107–112, 2005, doi: 10.1002/adfm.200400044.

[26] J. Janek and W. G. Zeier, “A solid future for battery development,” Nat. Energy, vol. 1, no. 9, pp. 1–4, 2016.

[27] V. Etacheri, R. Marom, R. Elazari, G. Salitra, and D. Aurbach, “Challenges in the development of advanced Li-ion batteries: A review,” Energy Environ. Sci., vol. 4, no. 9, pp. 3243–3262, 2011, doi: 10.1039/c1ee01598b.

[28] H. D. Yoo, E. Markevich, G. Salitra, D. Sharon, and D. Aurbach, “On the challenge of developing advanced technologies for electrochemical energy storage and conversion,” Mater. Today, vol. 17, no. 3, pp. 110–121, 2014, doi: 10.1016/j.mattod.2014.02.014.

[29] D. Starkman, M. M. Hamilton, and R. Chittum, The Best Business Writing 2014. Columbia University Press, 2014.

[30] A. Mauger, C. M. Julien, A. Paolella, M. Armand, and K. Zaghib, “Building better batteries in the solid state: a review,” Materials (Basel)., vol. 12, no. 23, p. 3892, 2019.

[31] S. Kumazaki et al., “High lithium ion conductive Li7La3Zr 2O12 by inclusion of both Al and Si,” Electrochem. commun., vol. 13, no. 5, pp. 509–512, 2011, doi: 10.1016/j.elecom.2011.02.035.

[32] J. L. Allen, J. Wolfenstine, E. Rangasamy, and J. Sakamoto, “Effect of substitution (Ta, Al, Ga) on the conductivity of Li7La3Zr2O12,” J. Power Sources, vol. 206, pp. 315–319, 2012.

[33] Y. Li, C. A. Wang, H. Xie, J. Cheng, and J. B. Goodenough, “High lithium ion conduction in garnet-type Li6La 3ZrTaO12,” Electrochem. commun., vol. 13, no. 12, pp. 1289–1292, 2011, doi: 10.1016/j.elecom.2011.07.008.

[34] J. Tippens et al., “Visualizing Chemomechanical Degradation of a Solid-State Battery Electrolyte,” ACS Energy Lett., vol. 4, no. 6, pp. 1475–1483, 2019, doi: 10.1021/acsenergylett.9b00816.

[35] Y.-F. Y. Yao and J. T. Kummer, “Ion exchange properties of and rates of ionic diffusion in beta-alumina,” J. Inorg. Nucl. Chem., vol. 29, no. 9, pp. 2453–2475, 1967.

[36] C. Galven, J. Dittmer, E. Suard, F. Le Berre, and M. P. Crosnier-Lopez, “Instability of lithium garnets against moisture. Structural characterization and dynamics of Li 7-xH xLa 3Sn 2O 12 and Li 5-xH xLa 3Nb 2O 12,” Chem. Mater., vol. 24, no. 17, pp. 3335–3345, 2012, doi: 10.1021/cm300964k.

[37] R. Murugan, W. Weppner, P. Schmid-Beurmann, and V. Thangadurai, “Structure and lithium ion conductivity of bismuth containing lithium garnets Li5La3Bi2O12 and Li6SrLa2Bi2O12,” Mater. Sci. Eng. B Solid-State Mater. Adv. Technol., vol. 143, no. 1–3, pp. 14–20, 2007, doi: 10.1016/j.mseb.2007.07.009.

[38] T. Zaiß, M. Ortner, R. Murugan, and W. Weppner, “Fast ionic conduction in cubic hafnium garnet Li7La3Hf2O12,” Ionics (Kiel)., vol. 16, no. 9, pp. 855–858, 2010, doi: 10.1007/s11581-010-0486-2.

[39] U. Ahmadu, Ŝ. Tomas, S. A. Jonah, A. O. Musa, and N. Rabiu, “Equivalent circuit models and analysis of impedance spectra of solid electrolyte.”

[40] E. J. Cussen, “Structure and ionic conductivity in lithium garnets,” J. Mater. Chem., vol. 20, no. 25, pp. 5167–5173, 2010.

[41] J. Awaka, N. Kijima, Y. Takahashi, H. Hayakawa, and J. Akimoto, “Synthesis and crystallographic studies of garnet-related lithium-ion conductors Li6CaLa2Ta2O12 and Li6BaLa2Ta2O12,” Solid State Ionics, vol. 180, no. 6–8, pp. 602–606, 2009, doi: 10.1016/j.ssi.2008.10.022.

[42] V. Thangadurai, H. Kaack, and W. J. F. Weppner, “Novel fast lithium ion conduction in garnet-type Li5La3M2O12 (M = Nb, Ta),” J. Am. Ceram. Soc., vol. 86, no. 3, pp. 437–440, 2003, doi: 10.1111/j.1151-2916.2003.tb03318.x.

[43] P. Knauth, “Inorganic solid Li ion conductors: An overview,” Solid State Ionics, vol. 180, no. 14–16, pp. 911–916, 2009, doi: 10.1016/j.ssi.2009.03.022.

[44] J. W. Fergus, “Ceramic and polymeric solid electrolytes for lithium-ion batteries,” J. Power Sources, vol. 195, no. 15, pp. 4554–4569, 2010, doi: 10.1016/j.jpowsour.2010.01.076.

[45] C. Liu, Z. Y. Wen, and K. Rui, “High ion conductivity in garnet-type F-doped Li7La3Zr2O12,” Wuji Cailiao Xuebao/Journal Inorg. Mater., vol. 30, no. 9, pp. 995–1001, 2015, doi: 10.15541/jim20150163.

[46] Y. Kato et al., “High-power all-solid-state batteries using sulfide superionic conductors,” Nat. Energy, vol. 1, no. 4, pp. 1–7, 2016.

[47] Y. Li, J.-T. Han, C.-A. Wang, H. Xie, and J. B. Goodenough, “Optimizing Li+ conductivity in a garnet framework,” J. Mater. Chem., vol. 22, no. 30, pp. 15357–15361, 2012.

[48] P. Zhao et al., “Self-consolidation mechanism and its application in the preparation of Al-doped cubic Li7La3Zr2O12,” Mater. Des., vol. 139, pp. 65–71, 2018, doi: 10.1016/j.matdes.2017.10.067.

[49] N. Jagjit, Handbook of solid state batteries, vol. 6. World Scientific, 2015.

[50] R. Murugan, V. Thangadurai, and W. Weppner, “Fast lithium ion conduction in garnet-type Li7La 3Zr2O12,” Angew. Chemie - Int. Ed., vol. 46, no. 41, pp. 7778–7781, 2007, doi: 10.1002/anie.200701144.

[51] L. Kong, I. Karatchevtseva, D. J. Gregg, M. G. Blackford, R. Holmes, and G. Triani, “A novel chemical route to prepare La 2 Zr 2 O 7 pyrochlore,” J. Am. Ceram. Soc., vol. 96, no. 3, pp. 935–941, 2013.

[52] Y. Lu, X. Meng, J. A. Alonso, M. T. Fernández-Díaz, and C. Sun, “Effects of Fluorine Doping on Structural and Electrochemical Properties of Li 6.25 Ga 0.25 La 3 Zr 2 O 12 as Electrolytes for Solid-State Lithium Batteries,” ACS Appl. Mater. Interfaces, vol. 11, no. 2, pp. 2042–2049, 2019, doi: 10.1021/acsami.8b17656.

[53] R. P. Rao, W. Gu, N. Sharma, V. K. Peterson, M. Avdeev, and S. Adams, “In situ neutron diffraction monitoring of Li7La3Zr2O12 formation: Toward a rational synthesis of garnet solid electrolytes.,” Chem. Mater., vol. 27, no. 8, pp. 2903–2910, 2015, doi: 10.1021/acs.chemmater.5b00149.

[54] X. Han et al., “Negating interfacial impedance in garnet-based solid-state Li metal batteries,” Nat. Mater., vol. 16, no. 5, pp. 572–579, 2017.

[55] K. Kerman, A. Luntz, V. Viswanathan, Y.-M. Chiang, and Z. Chen, “practical challenges hindering the development of solid state Li ion batteries,” J. Electrochem. Soc., vol. 164, no. 7, p. A1731, 2017.

[56] A. Sharafi, H. M. Meyer, J. Nanda, J. Wolfenstine, and J. Sakamoto, “Characterizing the Li-Li7La3Zr2O12 interface stability and kinetics as a function of temperature and current density,” J. Power Sources, vol. 302, pp. 135–139, 2016, doi: 10.1016/j.jpowsour.2015.10.053.

[57] S. Matthews and A. Powell, “Electrical conductivity vigour test: physiological basis and use,” Seed Test. Int., vol. 131, pp. 32–35, 2006.

[58] M. Koentopp, C. Chang, K. Burke, and R. Car, “Density functional calculations of nanoscale conductance,” J. Phys. Condens. Matter, vol. 20, no. 8, p. 83203, 2008.

[59] T. E. Toolbox, “Young’s Modulus—Tensile and Yield Strength for common Materials.” Engineering ToolBox United States, 2003.

[60] J. C. Bachman et al., “Inorganic Solid-State Electrolytes for Lithium Batteries: Mechanisms and Properties Governing Ion Conduction,” Chem. Rev., vol. 116, no. 1, pp. 140–162, 2016, doi: 10.1021/acs.chemrev.5b00563.

[61] K. Xu, “Nonaqueous liquid electrolytes for lithium-based rechargeable batteries,” Chem. Rev., vol. 104, no. 10, pp. 4303–4417, 2004, doi: 10.1021/cr030203g.

[62] J. B. Goodenough, “Oxide-ion electrolytes,” Annu. Rev. Mater. Res., vol. 33, no. 1, pp. 91–128, 2003.

[63] D. B. McWhan, S. J. Allen Jr, J. P. Remeika, and P. D. Dernier, “Ion-Ion Correlations and Diffusion in β-Alumina,” Phys. Rev. Lett., vol. 35, no. 14, p. 953, 1975.

[64] B. Andriyevsky, K. Doll, and T. Jacob, “Ab initio molecular dynamics study of lithium diffusion in tetragonal Li7La3Zr2O12,” Mater. Chem. Phys., vol. 185, pp. 210–217, 2017, doi: 10.1016/j.matchemphys.2016.10.025.

[65] M. Bitzer, T. Van Gestel, S. Uhlenbruck, and Hans-Peter-Buchkremer, “Sol-gel synthesis of thin solid Li7La3Zr2O12 electrolyte films for Li-ion batteries,” Thin Solid Films, vol. 615, pp. 128–134, 2016, doi: 10.1016/j.tsf.2016.07.010.

[66] V. Thangadurai and W. Weppner, “Li6ALa2Nb2O12 (A = Ca, Sr, Ba): A new class of fast lithium ion conductors with garnet-like structure,” J. Am. Ceram. Soc., vol. 88, no. 2, pp. 411–418, 2005, doi: 10.1111/j.1551-2916.2005.00060.x.

[67] B. Scrosati, K. M. Abraham, W. A. van Schalkwijk, and J. Hassoun, Lithium batteries: advanced technologies and applications, vol. 58. John Wiley & Sons, 2013.

[68] Z. Guo, D. Zhou, X. Dong, Z. Qiu, Y. Wang, and Y. Xia, “Ordered hierarchical mesoporous/macroporous carbon: A high-performance catalyst for rechargeable li-o2 batteries,” Adv. Mater., vol. 25, no. 39, pp. 5668–5672, 2013, doi: 10.1002/adma.201302459.

[69] P. Arora, R. E. White, and M. Doyle, “Capacity Fade Mechanisms and Side Reactions in Lithium-Ion Batteries,” J. Electrochem. Soc., vol. 145, no. 10, pp. 3647–3667, 1998, doi: 10.1149/1.1838857.

[70] N. L. À. O. Batteries, “Vertically Aligned N - Doped Coral-like Carbon Fiber Arrays as E ffi cient Air Electrodes for High-Performance,” ACS Nano, vol. 8, no. 3, pp. 3015–3022, 2014, [Online]. Available: http://pubs.acs.org/doi/abs/10.1021/nn500327p.

[71] R. Darling and J. Newman, “Modeling Side Reactions in Composite Li y Mn2 O 4 Electrodes,” J. Electrochem. Soc., vol. 145, no. 3, pp. 990–998, 1998, doi: 10.1149/1.1838376.

[72] C. Tubandt, “Über Elektrizitätsleitung in festen kristallisierten Verbindungen. Zweite Mitteilung. Überführung und Wanderung der Ionen in einheitlichen festen Elektrolyten,” Zeitschrift für Anorg. und Allg. Chemie, vol. 115, no. 1, pp. 105–126, 1921.

[73] J. B. Goodenough, H.-P. Hong, and J. A. Kafalas, “Fast Na+-ion transport in skeleton structures,” Mater. Res. Bull., vol. 11, no. 2, pp. 203–220, 1976.

[74] A. B. Yaroslavtsev, “Solid electrolytes: main prospects of research and development,” Russ. Chem. Rev., vol. 85, no. 11, pp. 1255–1276, 2016, doi: 10.1070/rcr4634.

[75] Y. Liu et al., “Understanding and suppressing side reactions in Li-air batteries,” Mater. Chem. Front., vol. 1, no. 12, pp. 2495–2510, 2017, doi: 10.1039/c7qm00353f.

[76] S. Ohno et al., “Materials design of ionic conductors for solid state batteries,” Prog. Energy, vol. 2, no. 2, p. 022001, 2020, doi: 10.1088/2516-1083/ab73dd.

[77] J. Awaka, N. Kijima, K. Kataoka, H. Hayakawa, K. ichi Ohshima, and J. Akimoto, "Neutron powder diffraction study of tetragonal Li7La3Hf2O12 with the garnet-related type structure," J. Solid State Chem., vol. 183, no. 1, pp. 180–185, 2010, doi: 10.1016/j.jssc.2009.10.030.

[78] M. Kotobuki, K. Kanamura, Y. Sato, and T. Yoshida, "Fabrication of all-solid-state lithium battery with lithium metal anode using Al2O3-added Li7La3Zr 2O12 solid electrolyte," J. Power Sources, vol. 196, no. 18, pp. 7750–7754, 2011, doi: 10.1016/j.jpowsour.2011.04.047.

[79] D. O. Shin et al., "Synergistic multi-doping effects on the Li7La3Zr2O12 solid electrolyte for fast lithium ion conduction," Sci. Rep., vol. 5, pp. 1–9, 2015, doi: 10.1038/srep18053.

[80] L. J. Miara et al., "Effect of Rb and Ta doping on the ionic conductivity and stability of the garnet Li7+2x-y(La3-xRbx)(Zr 2-yTay)O12 ($0 \leq x \leq 0.375$, $0 \leq y \leq 1$) Superionic conductor: A first principles investigation," Chem. Mater., vol. 25, no. 15, pp. 3048–3055, 2013, doi: 10.1021/cm401232r.

[81] P. Zhao et al., "A novel method for preparation of high dense tetragonal Li7La3Zr2O12," J. Power Sources, vol. 344, pp. 56–61, 2017, doi: 10.1016/j.jpowsour.2017.01.088.

[82] K. H. Kim et al., "Characterization of the interface between LiCoO2 and Li 7La3Zr2O12 in an all-solid-state rechargeable lithium battery," J. Power Sources, vol. 196, no. 2, pp. 764–767, 2011, doi: 10.1016/j.jpowsour.2010.07.073.

[83] Y. Kim, H. Jo, J. L. Allen, H. Choe, J. Wolfenstine, and J. Sakamoto, "The Effect of Relative Density on the Mechanical Properties of Hot-Pressed Cubic Li 7 la 3 Zr 2 O 12," J. Am. Ceram. Soc., vol. 99, no. 4, pp. 1367–1374, 2016, doi: 10.1111/jace.14084.

[84] S. Ohta, J. Seki, Y. Yagi, Y. Kihira, T. Tani, and T. Asaoka, "Co-sinterable lithium garnet-type oxide electrolyte with cathode for all-solid-state lithium ion battery," J. Power Sources, vol. 265, pp. 40–44, 2014, doi: 10.1016/j.jpowsour.2014.04.065.

[85] Y. Jin and P. J. McGinn, "Al-doped Li7La3Zr2O12 synthesized by a polymerized complex method," J. Power Sources, vol. 196, no. 20, pp. 8683–8687, 2011.

[86] M. Huang, A. Dumon, and C. W. Nan, "Effect of Si, in and Ge doping on high ionic conductivity of Li 7La 3Zr 2O 12," Electrochem. commun., vol. 21, no. 1, pp. 62–64, 2012, doi: 10.1016/j.elecom.2012.04.032.

[87] G. Larraz, A. Orera, and M. L. Sanjuán, "Cubic phases of garnet-type $Li_7La_3Zr_2O_{12}$: the role of hydration," 2013.

[88] A. Düvel, A. Kuhn, L. Robben, M. Wilkening, and P. Heitjans, "Mechanosynthesis of solid electrolytes: Preparation, characterization, and li ion transport properties of garnet-type Al-doped Li 7La 3Zr 2O 12 crystallizing with cubic symmetry," J. Phys. Chem. C, vol. 116, no. 29, pp. 15192–15202, 2012, doi: 10.1021/jp301193r.

[89] V. Thangadurai, S. Adams, and W. Weppner, “Crystal structure revision and identification of Li+-ion migration pathways in the garnet-like Li5La3M 2O12 (M = Nb, Ta) oxides,” Chem. Mater., vol. 16, no. 16, pp. 2998–3006, 2004, doi: 10.1021/cm031176d.

[90] A. Ramzy and V. Thangadurai, “Tailor-made development of fast Li ion conducting garnet-like solid electrolytes,” ACS Appl. Mater. Interfaces, vol. 2, no. 2, pp. 385–390, 2010, doi: 10.1021/am900643t.

[91] R. Murugan, W. Weppner, P. Schmid-Beurmann, and V. Thangadurai, “Structure and lithium ion conductivity of garnet-like Li5La3Sb2O12 and Li6SrLa2Sb2O12,” Mater. Res. Bull., vol. 43, no. 10, pp. 2579–2591, 2008, doi: 10.1016/j.materresbull.2007.10.035.

[92] V. Thangadurai and W. Weppner, “Investigations on electrical conductivity and chemical compatibility between fast lithium ion conducting garnet-like Li6BaLa2Ta2O12 and lithium battery cathodes,” J. Power Sources, vol. 142, no. 1–2, pp. 339–344, 2005.

[93] D. Rettenwander et al., “DFT study of the role of Al3+ in the fast ion-conductor Li 7-3xAl3+xLa3Zr2O 12 garnet,” Chem. Mater., vol. 26, no. 8, pp. 2617–2623, 2014, doi: 10.1021/cm5000999.

[94] H. Buschmann et al., “Structure and dynamics of the fast lithium ion conductor ‘li 7La3Zr2O12,’” Phys. Chem. Chem. Phys., vol. 13, no. 43, pp. 19378–19392, 2011, doi: 10.1039/c1cp22108f.

[95] W. Gu, M. Ezbiri, R. P. Rao, M. Avdeev, and S. Adams, “Effects of penta-and trivalent dopants on structure and conductivity of Li7La3Zr2O12,” Solid State Ionics, vol. 274, pp. 100–105, 2015.

[96] A. Kuhn, S. Narayanan, L. Spencer, G. Goward, V. Thangadurai, and M. Wilkening, “Li self-diffusion in garnet-type Li 7 La 3 Zr 2 O 12 as probed directly by diffusion-induced Li 7 spin-lattice relaxation NMR spectroscopy,” Phys. Rev. B, vol. 83, no. 9, p. 94302, 2011.

[97] W. Xue et al., “The effect of sintering process on lithium ionic conductivity of Li6.4Al0.2La3Zr2O12 garnet produced by solid-state synthesis,” RSC Adv., vol. 8, no. 24, pp. 13083–13088, 2018, doi: 10.1039/c8ra01329b.

[98] M. Rawlence, I. Garbayo, S. Buecheler, and J. L. M. Rupp, “On the chemical stability of post-lithiated garnet Al-stabilized Li7La3Zr2O12 solid state electrolyte thin films,” Nanoscale, vol. 8, no. 31, pp. 14746–14753, 2016, doi: 10.1039/c6nr04162k.

[99] J. Awaka, N. Kijima, H. Hayakawa, and J. Akimoto, “Synthesis and structure analysis of tetragonal Li7La3Zr2O12 with the garnet-related type structure,” J. Solid State Chem., vol. 182, no. 8, pp. 2046–2052, 2009, doi: 10.1016/j.jssc.2009.05.020.

[100] H. Xie, J. A. Alonso, Y. Li, M. T. Fernández-Díaz, and J. B. Goodenough, “Lithium distribution in aluminum-free cubic Li7La3Zr2O12,” Chem. Mater., vol. 23, no. 16, pp. 3587–3589, 2011.

[101] H. Xie, Y. Li, and J. B. Goodenough, “Low-temperature synthesis of Li 7La 3Zr 2O 12 with cubic garnet-type structure,” Mater. Res. Bull., vol. 47, no. 5, pp. 1229–1232, 2012, doi: 10.1016/j.materresbull.2012.01.027.

[102] I. N. David, T. Thompson, J. Wolfenstine, J. L. Allen, and J. Sakamoto, “Microstructure and li-ion conductivity of hot-pressed cubic Li7la3Zr2O12,” J. Am. Ceram. Soc., vol. 98, no. 4, pp. 1209–1214, 2015, doi: 10.1111/jace.13455.

[103] M. Matsui et al., “Phase stability of a garnet-type lithium ion conductor Li 7La3Zr2O12,” Dalt. Trans., vol. 43, no. 3, pp. 1019–1024, 2014, doi: 10.1039/c3dt52024b.

[104] M. Matsui et al., “Phase stability of a garnet-type lithium ion conductor Li 7 La 3 Zr 2 O 12,” Dalt. Trans., vol. 43, no. 3, pp. 1019–1024, 2014.

[105] K. Tadanaga et al., “Preparation of lithium ion conductive Al-doped Li7La3Zr2O12 thin films by a sol-gel process,” J. Power Sources, vol. 273, pp. 844–847, 2015, doi: 10.1016/j.jpowsour.2014.09.164.

[106] V. Thangadurai, S. Narayanan, and D. Pinzaru, “Garnet-type solid-state fast Li ion conductors for Li batteries: Critical review,” Chem. Soc. Rev., vol. 43, no. 13, pp. 4714–4727, 2014, doi: 10.1039/c4cs00020j.

[107] C. Bernuy-Lopez, W. Manalastas, J. M. Lopez Del Amo, A. Aguadero, F. Aguesse, and J. A. Kilner, “Atmosphere controlled processing of ga-substituted garnets for high li-ion conductivity ceramics,” Chem. Mater., vol. 26, no. 12, pp. 3610–3617, 2014, doi: 10.1021/cm5008069.

[108] C. Deviannapoorani, L. Dhivya, S. Ramakumar, and R. Murugan, “Lithium ion transport properties of high conductive tellurium substituted Li7La3Zr2O12 cubic lithium garnets,” J. Power Sources, vol. 240, pp. 18–25, 2013, doi: 10.1016/j.jpowsour.2013.03.166.

[109] R. J. Chen, M. Huang, W. Z. Huang, Y. Shen, Y. H. Lin, and C. W. Nan, “Effect of calcining and Al doping on structure and conductivity of Li 7La3Zr2O12,” Solid State Ionics, vol. 265, pp. 7–12, 2014, doi: 10.1016/j.ssi.2014.07.004.

[110] L. Cheng et al., “Effect of surface microstructure on electrochemical performance of garnet solid electrolytes,” ACS Appl. Mater. Interfaces, vol. 7, no. 3, pp. 2073–2081, 2015, doi: 10.1021/am508111r.

[111] L. Cheng et al., “Effect of microstructure and surface impurity segregation on the electrical and electrochemical properties of dense Al-substituted Li7La 3Zr2O12,” J. Mater. Chem. A, vol. 2, no. 1, pp. 172–181, 2014, doi: 10.1039/c3ta13999a.

[112] I. Kokal, M. Somer, P. H. L. Notten, and H. T. Hintzen, “Sol-gel synthesis and lithium ion conductivity of Li7La 3Zr2O12 with garnet-related type structure,” Solid State Ionics, vol. 185, no. 1, pp. 42–46, 2011, doi: 10.1016/j.ssi.2011.01.002.

[113] D. Rettenwander et al., “DFT study of the role of Al3+ in the fast ion-conductor Li7–3 x Al3+ x La3Zr2O12 garnet,” Chem. Mater., vol. 26, no. 8, pp. 2617–2623, 2014.

[114] Y. Li et al., “W-Doped Li7La3Zr2O12 Ceramic Electrolytes for Solid State Li-ion Batteries Electrochimica Acta W-Doped Li 7 La 3 Zr 2 O 12 Ceramic Electrolytes for Solid State Li-ion Batteries,” Electrochim. Acta, vol. 180, no. October 2015, pp. 37–42, 2018, [Online]. Available: http://dx.doi.org/10.1016/j.electacta.2015.08.046.

[115] H. Katsui and T. Goto, “Preparation of cubic and tetragonal Li7La3Zr2O12 film by metal organic chemical vapor deposition,” Thin Solid Films, vol. 584, pp. 130–134, 2015, doi: 10.1016/j.tsf.2014.11.094.

[116] Y. Li, C.-A. Wang, H. Xie, J. Cheng, and J. B. Goodenough, “High lithium ion conduction in garnet-type Li6La3ZrTaO12,” Electrochem. commun., vol. 13, no. 12, pp. 1289–1292, 2011.

[117] D. Rettenwander et al., “Synthesis, Crystal Chemistry, and Electrochemical Properties of Li7-2xLa3Zr2-xMoxO12 (x = 0.1-0.4): Stabilization of the Cubic Garnet Polymorph via Substitution of Zr4+ by Mo6+,” Inorg. Chem., vol. 54, no. 21, pp. 10440–10449, 2015, doi: 10.1021/acs.inorgchem.5b01895.

[118] D. O. Shin et al., “Synergistic multi-doping effects on the Li 7 La 3 Zr 2 O 12 solid electrolyte for fast lithium ion conduction,” Sci. Rep., vol. 5, p. 18053, 2015.

[119] C. A. Geiger et al., “Crystal chemistry and stability of ‘Li7La 3Zr2O12’ garnet: A fast lithium-ion conductor,” Inorg. Chem., vol. 50, no. 3, pp. 1089–1097, 2011, doi: 10.1021/ic101914e.

[120] M. Kotobuki, K. Kanamura, Y. Sato, and T. Yoshida, “Fabrication of all-solid-state lithium battery with lithium metal anode using Al2O3-added Li7La3Zr2O12 solid electrolyte,” J. Power Sources, vol. 196, no. 18, pp. 7750–7754, 2011.

[121] C. Liu and Z. Wen, “Fluorine-containing lithium-garnet-type oxide ceramics.” Google Patents, Apr. 30, 2015.

[122] S. R. Yeandel, B. J. Chapman, P. R. Slater, and P. Goddard, “Structure and Lithium-Ion Dynamics in Fluoride-Doped Cubic Li 7 La 3 Zr 2 O 12 (LLZO) Garnet for Li Solid-State Battery Applications,” J. Phys. Chem. C, vol. 122, no. 49, pp. 27811–27819, 2018, doi: 10.1021/acs.jpcc.8b07704.

[123] C. Liu, K. Rui, C. Shen, M. E. Badding, G. Zhang, and Z. Wen, “Reversible ion exchange and structural stability of garnet-type Nb-doped Li7La3Zr2O12 in water for applications in lithium batteries,” J. Power Sources, vol. 282, pp. 286–293, 2015.

[124] M. A. Howard et al., “Effect of Ga incorporation on the structure and Li ion conductivity of La 3 Zr 2 Li 7 O 12,” Dalt. Trans., vol. 41, no. 39, pp. 12048–12053, 2012.

[125] M. A. Howard et al., “Synthesis, conductivity and structural aspects of Nd 3 Zr 2 Li 7− 3x Al x O 12,” J. Mater. Chem. A, vol. 1, no. 44, pp. 14013–14022, 2013.

[126] J. Percival, E. Kendrick, R. I. Smith, and P. R. Slater, “Cation ordering in Li containing garnets: synthesis and structural characterisation of the tetragonal system, Li 7 La 3 Sn 2 O 12,” Dalt. Trans., no. 26, pp. 5177–5181, 2009.

[127] G. Larraz, A. Orera, and M. L. Sanjuán, “Cubic phases of garnet-type Li7La3Zr 2O12: The role of hydration,” J. Mater. Chem. A, vol. 1, no. 37, pp. 11419–11428, 2013, doi: 10.1039/c3ta11996c.

[128] Y. Chen, E. Rangasamy, C. R. dela Cruz, C. Liang, and K. An, “A study of suppressed formation of low-conductivity phases in doped Li 7 La 3 Zr 2 O 12 garnets by in situ neutron diffraction,” J. Mater. Chem. A, vol. 3, no. 45, pp. 22868–22876, 2015.

[129] X. Li et al., “Rational design of strontium antimony co-doped Li7La3Zr2O12 electrolyte membrane for solid-state lithium batteries,” J. Alloys Compd., vol. 794, pp. 347–357, 2019, doi: 10.1016/j.jallcom.2019.04.274.

[130] Z. F. Yow, Y. L. Oh, W. Gu, R. P. Rao, and S. Adams, “Effect of Li+/H+ exchange in water treated Ta-doped Li7La3Zr2O12,” Solid State Ionics, vol. 292, pp. 122–129, 2016, doi: 10.1016/j.ssi.2016.05.016.

[131] J. Zhang et al., “High-voltage and free-standing poly(propylene carbonate)/Li6.75La3Zr1.75Ta0.25O12 composite solid electrolyte for wide temperature range and flexible solid lithium ion battery,” J. Mater. Chem. A, vol. 5, no. 10, pp. 4940–4948, 2017, doi: 10.1039/c6ta10066j.

[132] “High lithium ion conductive Li7La3Zr2O12 by inclusion of both Al and Si,” Electrochem. commun., vol. 13, no. 5, pp. 509–512, 2011.

[133] L. J. Miara, W. D. Richards, Y. E. Wang, and G. Ceder, “First-Principles Studies on Cation Dopants and Electrolyte|Cathode Interphases for Lithium Garnets,” Chem. Mater., vol. 27, no. 11, pp. 4040–4047, 2015, doi: 10.1021/acs.chemmater.5b01023.

[134] S. Ramakumar, L. Satyanarayana, S. V. Manorama, and R. Murugan, “Structure and Li+ dynamics of Sb-doped Li7La 3Zr2O12 fast lithium ion conductors,” Phys. Chem. Chem. Phys., vol. 15, no. 27, pp. 11327–11338, 2013, doi: 10.1039/c3cp50991e.

[135] K. Hoshina, K. Yoshima, M. Kotobuki, and K. Kanamura, “Fabrication of LiNi 0.5Mn 1.5O 4 thin film cathode by PVP sol-gel process and its application of all-solid-state lithium ion batteries using Li 1 + xAl xTi 2 - X(PO 4) 3 solid electrolyte,” Solid State Ionics, vol. 209–210, pp. 30–35, 2012, doi: 10.1016/j.ssi.2011.12.018.

[136] Y. Zhu et al., “A surface-modified antiperovskite as an electrocatalyst for water oxidation,” Nat. Commun., vol. 9, no. 1, 2018, doi: 10.1038/s41467-018-04682-y.

[137] X. Huang and J. Hitt, “Lithium ion battery separators: Development and performance characterization of a composite membrane,” J. Memb. Sci., vol. 425–426, pp. 163–168, 2013, doi: 10.1016/j.memsci.2012.09.027.

[138] E. J. Cussen, “The structure of lithium garnets: Cation disorder and clustering in a new family of fast Li+ conductors,” Chem. Commun., no. 4, pp. 412–413, 2006, doi: 10.1039/b514640b.

[139] E. J. Cussen and T. W. S. Yip, “A neutron diffraction study of the d0 and d10 lithium garnets Li3Nd3W2O12 and Li5La3Sb2O12,” J. Solid State Chem., vol. 180, no. 6, pp. 1832–1839, 2007, doi: 10.1016/j.jssc.2007.04.007.

[140] L. Dhivya, N. Janani, B. Palanivel, and R. Murugan, “Li+ transport properties of W substituted Li7La 3Zr2O12 cubic lithium garnets,” AIP Adv., vol. 3, no. 8, 2013, doi: 10.1063/1.4818971.

[141] N. Imanishi, “Solid electrolytes for aqueous lithium air batteries,” in The Lithium Air Battery, Springer, 2014, pp. 215–234.

[142] M. Zhang et al., “Water-stable lithium anode with Li1.4Al0.4Ge 1.6(PO4)3-TiO2 sheet prepared by tape casting method for lithium-air batteries,” J. Power Sources, vol. 235, pp. 117–121, 2013, doi: 10.1016/j.jpowsour.2013.01.167.

[143] Y. Wang and W. Lai, “Phase transition in lithium garnet oxide ionic conductors Li7La3Zr2O12: The role of Ta substitution and H2O/CO2 exposure,” J. Power Sources, vol. 275, pp. 612–620, 2015, doi: 10.1016/j.jpowsour.2014.11.062.

[144] Y. Jin and P. J. McGinn, “Li7La3Zr2O12 electrolyte stability in air and fabrication of a Li/Li7La3Zr 2O12/Cu0.1V2O5 solid-state battery,” J. Power Sources, vol. 239, pp. 326–331, 2013, doi: 10.1016/j.jpowsour.2013.03.155.

[145] M. Nyman, T. M. Alam, S. K. McIntyre, G. C. Bleier, and D. Ingersoll, “Alternative approach to increasing Li mobility in Li-La-Nb/Ta garnet electrolytes,” Chem. Mater., vol. 22, no. 19, pp. 5401–5410, 2010, doi: 10.1021/cm101438x.

[146] C. Galven, J.-L. Fourquet, M.-P. Crosnier-Lopez, and F. Le Berre, “Instability of the lithium garnet Li7La3Sn2O12: Li+/H+ exchange and structural study,” Chem. Mater., vol. 23, no. 7, pp. 1892–1900, 2011.

[147] L. Truong, J. Colter, and V. Thangadurai, “Chemical stability of Li-stuffed garnet-type Li5 + xBa xLa3 - XTa2O12 (x = 0, 0.5, 1) in water: A comparative analysis with the Nb analogue,” Solid State Ionics, vol. 247–248, pp. 1–7, 2013, doi: 10.1016/j.ssi.2013.05.013.

[148] L. Truong and V. Thangadurai, “Soft-chemistry of garnet-type Li5+ xBaxLa 3-xNb2O12 (x = 0, 0.5, 1): Reversible H + ↔ Li+ ion-exchange reaction and their X-ray, 7Li MAS NMR, IR, and AC impedance spectroscopy characterization,” Chem. Mater., vol. 23, no. 17, pp. 3970–3977, 2011, doi: 10.1021/cm2015127.

[149] T. Ma et al., “Preparation of PVDF based blend microporous membranes for lithium ion batteries by thermally induced phase separation: I. Effect of PMMA on the membrane formation process and the properties,” J. Memb. Sci., vol. 444, pp. 213–222, 2013, doi: 10.1016/j.memsci.2013.05.028.

[150] B. S. Lalia, E. Guillen-Burrieza, H. A. Arafat, and R. Hashaikeh, “Fabrication and characterization of polyvinylidenefluoride-co-hexafluoropropylene (PVDF-HFP) electrospun membranes for direct contact membrane distillation,” J. Memb. Sci., vol. 428, pp. 104–115, 2013, doi: 10.1016/j.memsci.2012.10.061.

[151] T. Furukawa, Y. Hirakawa, H. Kondo, and T. Kanemura, “Dissolution behavior of lithium compounds in ethanol,” Nucl. Mater. Energy, vol. 9, pp. 286–291, 2016.

[152] E. Rangasamy, J. Wolfenstine, J. Allen, and J. Sakamoto, “The effect of 24c-site (A) cation substitution on the tetragonal–cubic phase transition in Li7− xLa3− xAxZr2O12 garnet-based ceramic electrolyte,” J. Power Sources, vol. 230, pp. 261–266, 2013.

[153] R. Murugan, V. Thangadurai, and W. Weppner, “Fast lithium ion conduction in garnet-type Li7La3Zr2O12,” Angew. Chemie Int. Ed., vol. 46, no. 41, pp. 7778–7781, 2007.

[154] Y. Zhang, F. Chen, R. Tu, Q. Shen, and L. Zhang, “Field assisted sintering of dense Al-substituted cubic phase Li 7La3Zr2O12 solid electrolytes,” J. Power Sources, vol. 268, pp. 960–964, 2014, doi: 10.1016/j.jpowsour.2014.03.148.

[155] T. Grygar, F. Marken, U. Schröder, and F. Scholz, “Electrochemical analysis of solids. A review,” Collect. Czechoslov. Chem. Commun., vol. 67, no. 2, pp. 163–208, 2002, doi: 10.1135/cccc20020163.

[156] R. A. Huggins, “Simple method to determine electronic conductivity and ionic components of the conductors in mixed a review,” Ionics (Kiel)., vol. 8, no. 3–4, pp. 300–313, 2002, doi: 10.1007/BF02376083.

[157] V. Thangadurai, R. A. Huggins, and W. Weppner, “Use of simple ac technique to determine the ionic and electronic conductivities in pure and Fe-substituted SrSnO3 perovskites,” J. Power Sources, vol. 108, no. 1–2, pp. 64–69, 2002, doi: 10.1016/S0378-7753(02)00002-2.

[158] J. Sunarso et al., “Mixed ionic-electronic conducting (MIEC) ceramic-based membranes for oxygen separation,” J. Memb. Sci., vol. 320, no. 1–2, pp. 13–41, 2008, doi: 10.1016/j.memsci.2008.03.074.

[159] H. Rickert, Electrochemistry of solids: an introduction, vol. 7. Springer Science & Business Media, 2012.

[160] W. Weppner and R. A. Huggins, “Electrochemical Methods for Determining Kinetic Properties of Solids,” Annu. Rev. Mater. Sci., vol. 8, no. 1, pp. 269–311, 1978, doi: 10.1146/annurev.ms.08.080178.001413.

[161] X. Yuan, H. Wang, J. Colin Sun, and J. Zhang, “AC impedance technique in PEM fuel cell diagnosis-A review,” Int. J. Hydrogen Energy, vol. 32, no. 17, pp. 4365–4380, 2007, doi: 10.1016/j.ijhydene.2007.05.036.

[162] Gramy Instruments Inc., “Basics of Electrochemical Impedance Spectroscopy Impedance Values,” Appl. Note Rev. 2.0, no. 215, pp. 1–28, 2014.

[163] A. K. Manohar, O. Bretschger, K. H. Nealson, and F. Mansfeld, “The use of electrochemical impedance spectroscopy (EIS) in the evaluation of the electrochemical properties of a microbial fuel cell,” Bioelectrochemistry, vol. 72, no. 2, pp. 149–154, 2008, doi: 10.1016/j.bioelechem.2008.01.004.

[164] P. Braun, C. Uhlmann, A. Weber, H. Störmer, D. Gerthsen, and E. Ivers-Tiffée, “Separation of the bulk and grain boundary contributions to the total conductivity of solid lithium-ion conducting electrolytes,” J. Electroceramics, vol. 38, no. 2–4, pp. 157–167, 2017, doi: 10.1007/s10832-016-0061-y.

[165] I. D. Raistrick, C. Ho, and R. A. Huggins, “Ionic conductivity of some lithium silicates and aluminosilicates,” J. Electrochem. Soc., vol. 123, no. 10, p. 1469, 1976.

[166] B. Horgan, “Investigating Grain Boundaries in BaCuS1-xSexF Using Impedance Spectroscopy,” Oregon Oregon State Univ., 2004.

[167] M. U. I. B. M. Rahimi, “X-ray Powder Diffraction (XRD),” 2020.

[168] J. M. Lee et al., “High lithium ion conductivity of Li7La3Zr 2O12 synthesized by solid state reaction,” Solid State Ionics, vol. 258, pp. 13–17, 2014, doi: 10.1016/j.ssi.2014.01.043.

[169] J. Jamnik and J. Maier, “Treatment of the Impedance of Mixed Conductors Equivalent Circuit Model and Explicit Approximate Solutions,” J. Electrochem. Soc., vol. 146, no. 11, pp. 4183–4188, 1999, doi: 10.1149/1.1392611.

[170] M. Kotobuki, H. Munakata, K. Kanamura, Y. Sato, and T. Yoshida, “Compatibility of Li[sub 7]La[sub 3]Zr[sub 2]O[sub 12] Solid Electrolyte to All-Solid-State Battery Using Li Metal Anode,” J. Electrochem. Soc., vol. 157, no. 10, p. A1076, 2010, doi: 10.1149/1.3474232.

[171] R. Jalem et al., “Concerted migration mechanism in the Li ion dynamics of garnet-type Li 7La3Zr2O12,” Chem. Mater., vol. 25, no. 3, pp. 425–430, 2013, doi: 10.1021/cm303542x.

[172] X. Xu, C. Su, W. Zhou, Y. Zhu, Y. Chen, and Z. Shao, “Co-doping strategy for developing perovskite oxides as highly efficient electrocatalysts for oxygen evolution reaction,” Adv. Sci., vol. 3, no. 2, pp. 1–6, 2015, doi: 10.1002/advs.201500187.

[173] S. Ohta, Y. Kihira, and T. Asaoka, “Grain Boundary Analysis of the Garnet-Like Oxides Li7+ X− YLa3− XAXZr2− YNbYO12 (A= Sr or Ca),” Front. Energy Res., vol. 4, p. 30, 2016.

[174] A. Logéat et al., “From order to disorder: The structure of lithium-conducting garnets Li7− xLa3TaxZr2− xO12 (x= 0–2),” Solid State Ionics, vol. 206, pp. 33–38, 2012.

[175] J. Maier, “Ionic conduction in space charge regions,” Prog. Solid State Chem., vol. 23, no. 3, pp. 171–263, 1995, doi: 10.1016/0079-6786(95)00004-E.

[176] P. Lupetin, G. Gregori, and J. Maier, “Mesoscopic Charge Carriers Chemistry in Nanocrystalline SrTiO3,” Angew. Chemie, vol. 122, no. 52, pp. 10321–10324, 2010, doi: 10.1002/ange.201003917.

[177] E. Fabbri, D. Pergolesi, and E. Traversa, “Ionic conductivity in oxide heterostructures: The role of interfaces,” Sci. Technol. Adv. Mater., vol. 11, no. 5, 2010, doi: 10.1088/1468-6996/11/5/054503.

[178] H. L. Tuller, “Ionic conduction in nanocrystalline materials,” Solid State Ionics, vol. 131, no. 1, pp. 143–157, 2000, doi: 10.1016/S0167-2738(00)00629-9.

[179] Z. Liu et al., “Anomalous high ionic conductivity of nanoporous β-Li 3PS4,” J. Am. Chem. Soc., vol. 135, no. 3, pp. 975–978, 2013, doi: 10.1021/ja3110895.

[180] P. Abelard and J. F. Baumard, “Study of the dc and ac electrical properties of an yttria-stabilized zirconia single crystal [(Z r O 2) 0.88-(Y 2 O 3) 0.12],” Phys. Rev. B, vol. 26, no. 2, p. 1005, 1982.

[181] J. E. Bauerle, “Study of solid electrolyte polarization by a complex admittance method,” J. Phys. Chem. Solids, vol. 30, no. 12, pp. 2657–2670, 1969.

[182] W. J. Bowman, J. Zhu, R. Sharma, and P. A. Crozier, “Electrical conductivity and grain boundary composition of Gd-doped and Gd/Pr co-doped ceria,” Solid State Ionics, vol. 272, pp. 9–17, 2015, doi: 10.1016/j.ssi.2014.12.006.

[183] S. Pandey, D. Kumar, O. Parkash, and L. Pandey, “Equivalent circuit models using CPE for impedance spectroscopy of electronic ceramics,” Integr. Ferroelectr., vol. 183, no. 1, pp. 141–162, 2017, doi: 10.1080/10584587.2017.1376984.

[184] A. K. Jonscher and K. Andrzej, “Dielectric Relaxation in Solids (Chelsea, London.” Dielectrics Press, 1983.

[185] K. Waetzig, C. Heubner, and M. Kusnezoff, “Reduced sintering temperatures of Li+ conductive Li1.3Al0.3Ti1.7(PO4)3 ceramics,” Crystals, vol. 10, no. 5, 2020, doi: 10.3390/cryst10050408.

[186] J.-F. Wu and X. Guo, “Origin of the low grain boundary conductivity in lithium ion conducting perovskites: Li 3x La 0.67− x TiO 3,” Phys. Chem. Chem. Phys., vol. 19, no. 8, pp. 5880–5887, 2017.

[187] C. Loho, R. Djenadic, M. Bruns, O. Clemens, and H. Hahn, “Garnet-type Li7La3Zr2O12 solid electrolyte thin films grown by CO2-laser assisted CVD for all-solid-state batteries,” J. Electrochem. Soc., vol. 164, no. 1, p. A6131, 2016.

[188] X. Wang, “Non-destructive characterisation of structural ceramics using impedance spectroscopy.” Brunel University School of Engineering and Design PhD Theses, 2001.

[189] Y. Wang, “Study of Garnet Type Electrolyte $Li_7La_3Zr_2O_{12}$ Structure and Electrochemical Performance,” 2019.

[190] M. P. O’Callaghan and E. J. Cussen, “The structure of the lithium-rich garnets Li6SrLa2M2O12 and Li6.4Sr1.4La1.6M2O12 (M = Sb, Ta),” Solid State Sci., vol. 10, no. 4, pp. 390–395, 2008, doi: 10.1016/j.solidstatesciences.2007.11.036.

[191] H. Hyooma and K. Hayashi, “Crystal structures of La3Li5M2O12 (M= Nb, Ta),” Mater. Res. Bull., vol. 23, no. 10, pp. 1399–1407, 1988.

[192] C.-Y. Yoo, S.-C. Kim, S.-S. Lee, and S.-J. Kim, “Synchrotron study of the garnet-type oxide Li6CaSm2Ta2O12,” Acta Crystallogr. Sect. E Struct. Reports Online, vol. 65, no. 11, pp. i74–i74, 2009.

[193] I. P. Roof, M. D. Smith, E. J. Cussen, and H. C. zur Loye, “Crystal growth of a series of lithium garnets Ln3Li5Ta2O12 (Ln=La, Pr, Nd): Structural properties, Alexandrite effect and unusual ionic conductivity,” J. Solid State Chem., vol. 182, no. 2, pp. 295–300, 2009, doi: 10.1016/j.jssc.2008.10.032.

[194] A. Mohammed and A. Abdullah, “Scanning Electron Microscopy (SEM): a Review,” Proc. 2018 Int. Conf. Hydraul. Pneum. - HERVEX, no. January, p. 85, 2018.

[195] K. D. Vernon-Parry, “Scanning electron microscopy: an introduction,” III-Vs Rev., vol. 13, no. 4, pp. 40–44, 2000.

APPENDIX

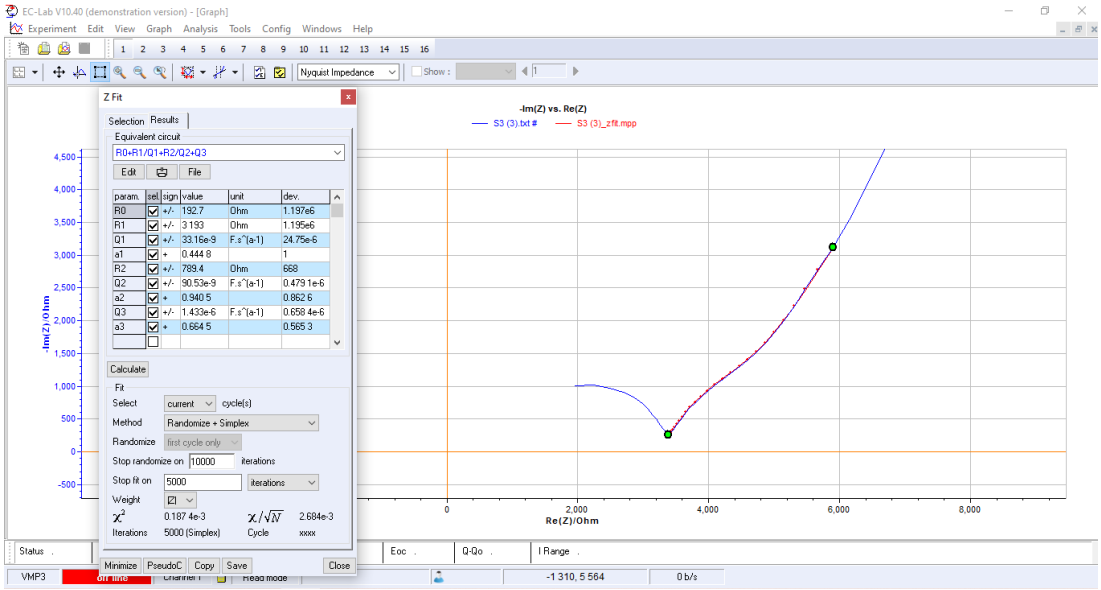

Figure A1. Impedance fitting of pure LLZO sample.

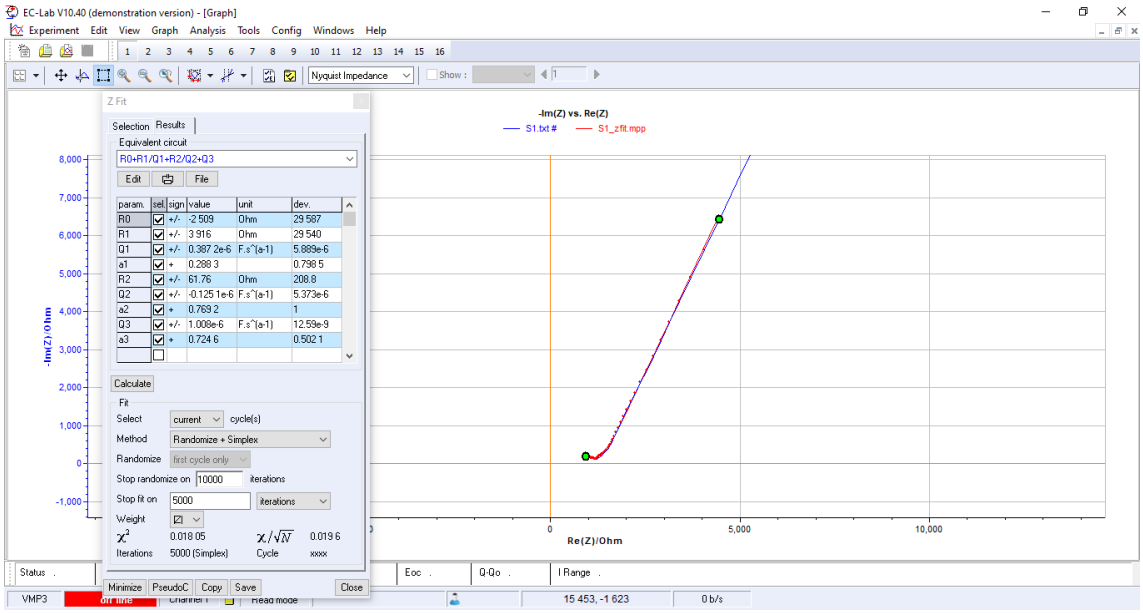

Figure A2. Impedance fitting of single-doped LLZO with Al sample.

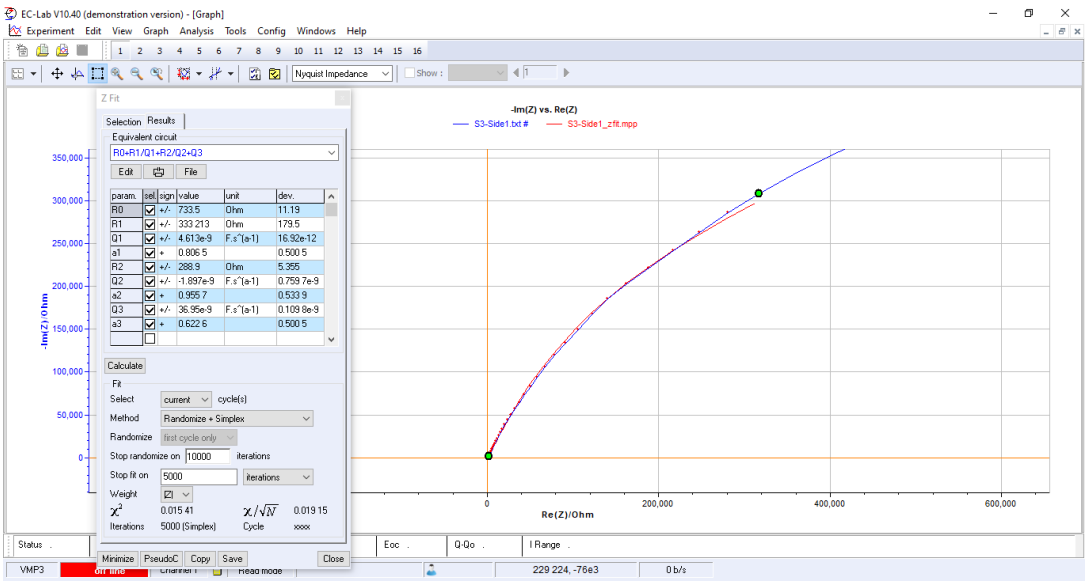

Figure A3. Impedance fitting of single-doped LLZO with F sample.

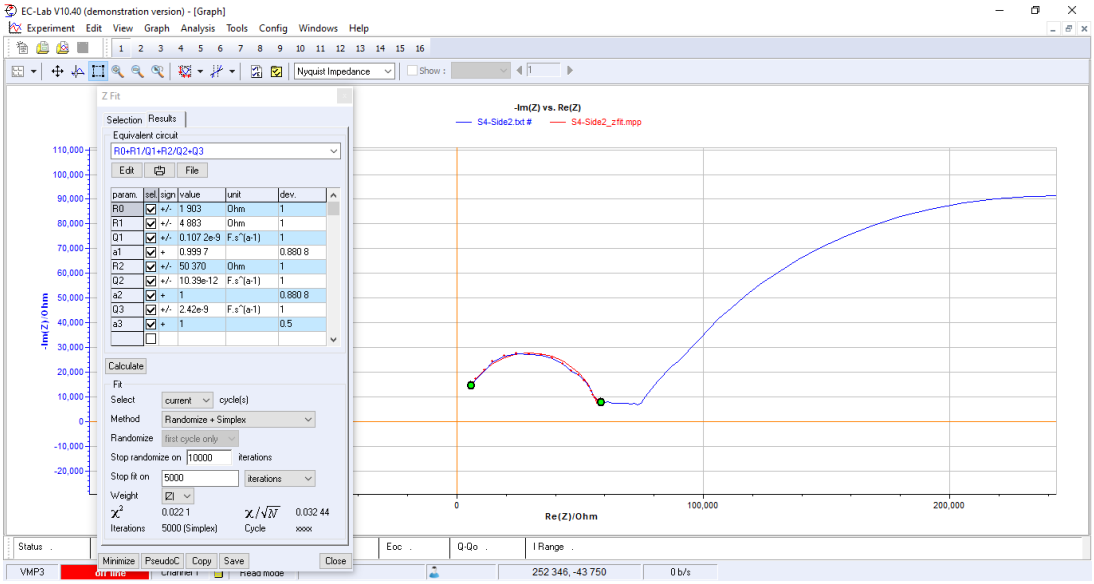

Figure A4. Impedance fitting of single-doped LLZO with Ta sample.

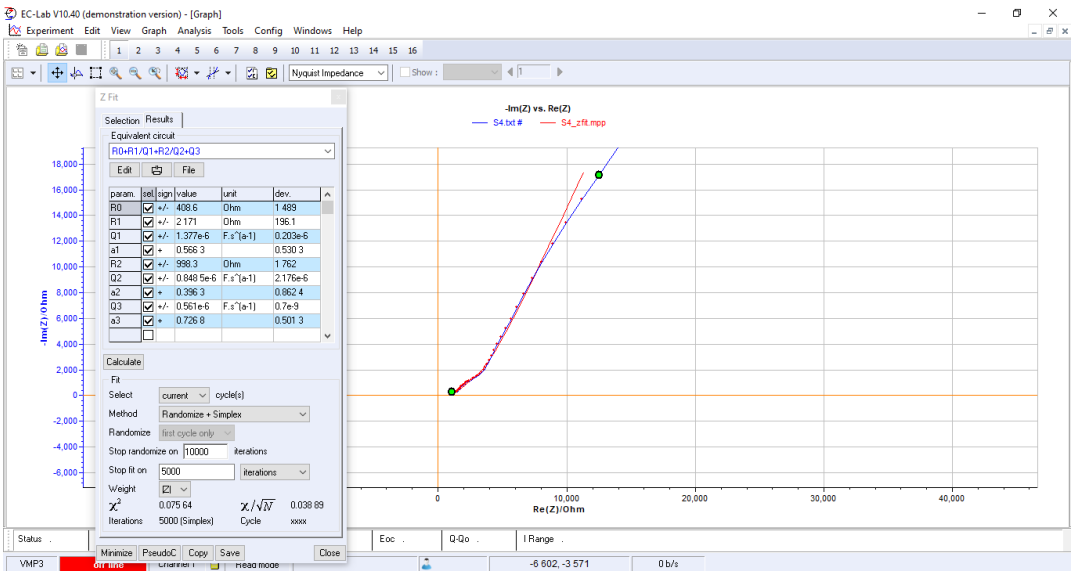

Figure A5. Impedance fitting of co-doped LLZO with Al and F sample.

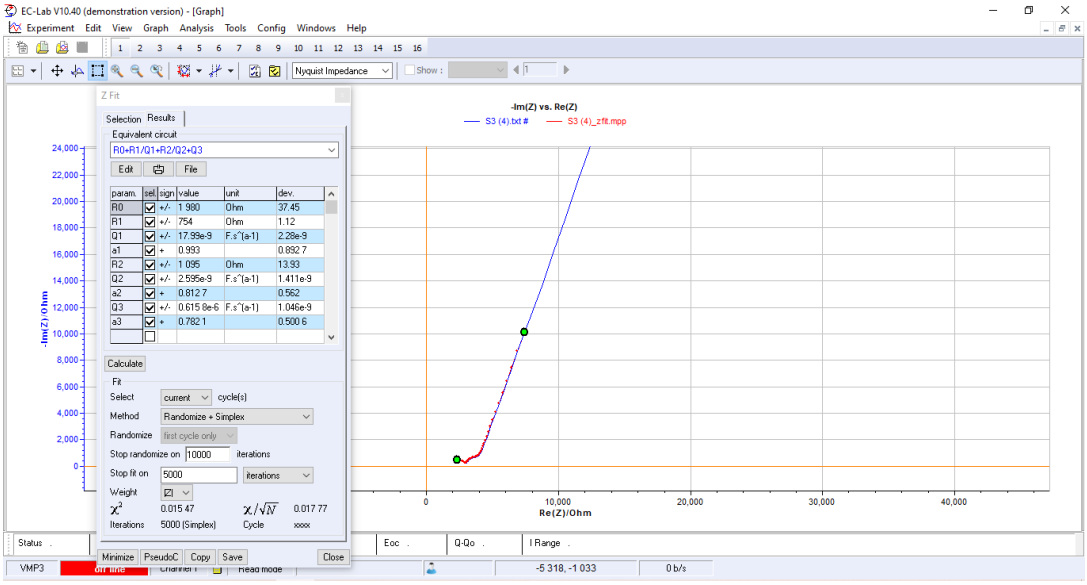

Figure A6. Impedance fitting of co-doped LLZO with Ta and F sample.

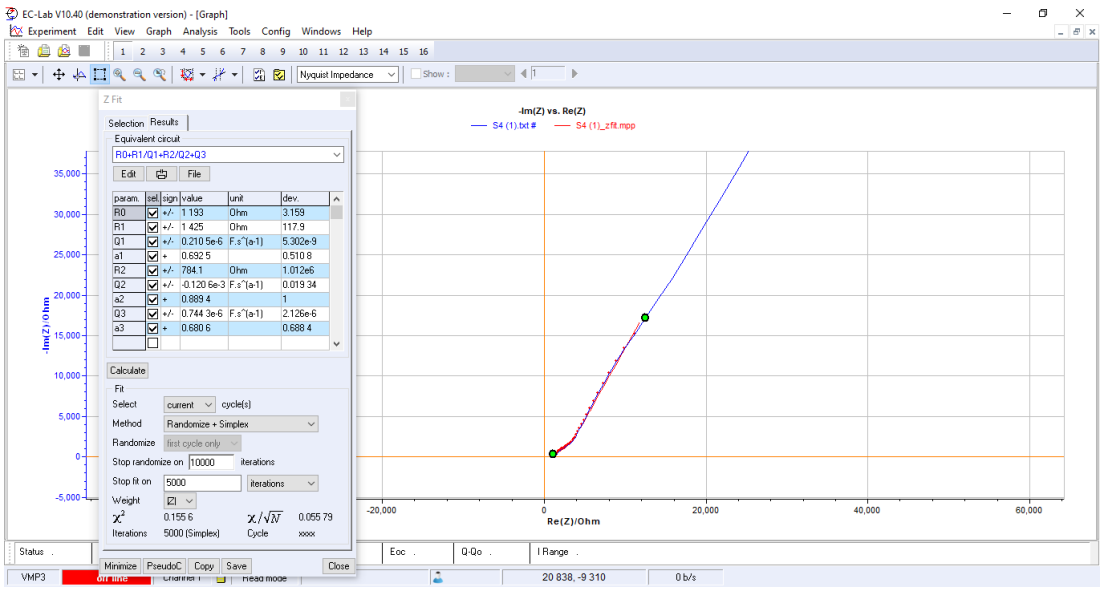

Figure A7. Impedance fitting of co-doped LLZO with Al and Ta sample.

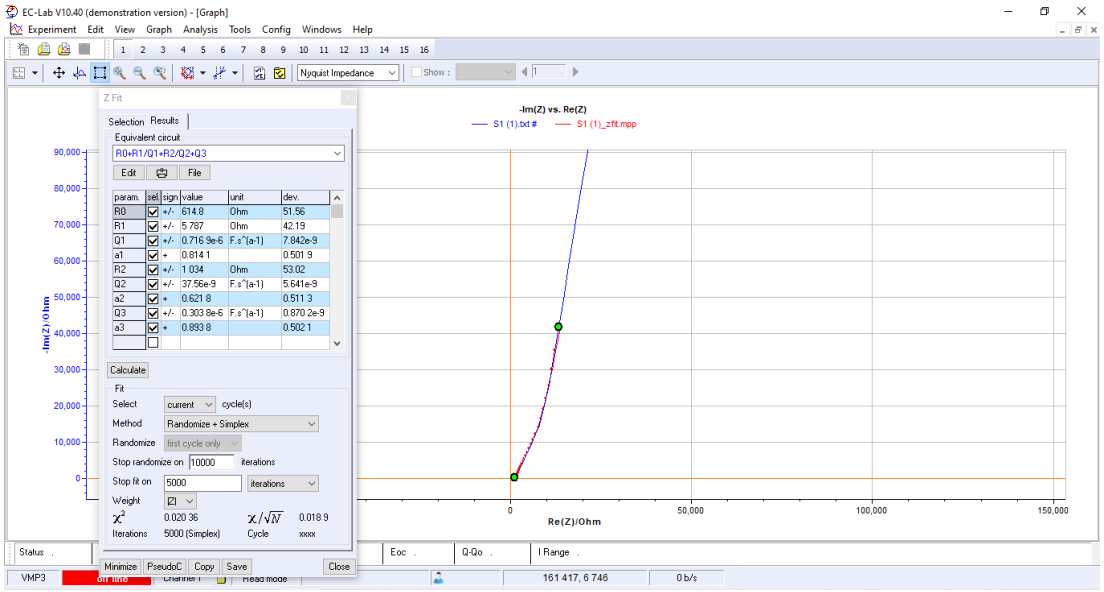

Figure A8. Impedance fitting of multi-doped LLZO with Al and Ta and F sample.